
Constructing and bounding the solutions of Quantum Gravity with the Event Horizon Telescope

Author:
Kolja Kuijpers

Supervisor:
Frank Saueressig

Abstract

Contrary to General Relativity, the gravitational theory of Quadratic Gravity is perturbatively renormalizable, and a candidate theory of quantum gravity as a result. Still, many features and intricacies of Quadratic Gravity as a classical theory are still unknown. In this thesis we provide a framework for generating static, spherically symmetric and asymptotically flat solutions to Quadratic Gravity, employing numerical methods. With this we are able to construct the phase of solutions and apply a newly introduced categorization to the solutions, distinguishing naked singularities, wormholes and the Schwarzschild solution. Solutions from each category are then used in simulating an elementary emission model of accreting matter. The resulting intensity profiles where then subjected to an in-depth analysis. Based on these results we can argue that observations like the ones by the Event Horizon Telescope can rule out certain parts of the phase space. Furthermore, we argue that there exist horizonless solutions which are virtually indistinguishable from a Schwarzschild black hole, indicating that on this basis alone a telescope cannot confirm whether it is looking at an event horizon or not. In this way, our work takes a first step to constructing the phase space of solution for Quadratic Gravity and bounding it through observations.

Department of High Energy Physics/IMAPP
Radboud University
Nijmegen, The Netherlands

August 13, 2022

CONTENTS

1	Introduction	2
2	The Merits of Quadratic Gravity	3
2.1	General Relativity	3
2.2	Extending beyond General Relativity	6
2.3	Quantum Gravity	7
2.4	Non-Renormalizability	8
3	Quadratic Gravity	11
3.1	The action	11
3.2	The equations of motion	11
3.3	Introducing a metric	12
3.4	Deriving analytical solution classes	12
3.5	Linearizing the equations of motion	14
4	Numerical Analysis of the Equations of Motion	16
4.1	Solution classes	16
4.2	Probing the Phase Space	19
4.3	Sensitivity on the Initial Radius r_i	24
4.4	Initial Conditions and Stress Energy Tensor	25
5	Probing the Geometry by Shadow Imaging	30
5.1	Intensity profiles	32
6	Summary	38
7	Outlook	40
7.1	Further investigation of the phase space	40
7.2	Imaging Type Ib solutions	40
7.3	Rotating solutions	41
7.4	Extending wormhole solutions	43
8	Acknowledgments	45
A	Variations of tensorial quantities	48
B	Mathematica	50
B.1	"Delta Fix" for explicitly defined indices in xCoba	50
C	Complete Expressions	51

1. INTRODUCTION

In the recent years humanity has kept on pushing the limits on what parts of the universe we can observe. The detection of gravitation waves by the LIGO collaboration in 2016 [1] was the first in a new observational window. Being predicted by Einstein a century ago, the confirmation of the existence of gravitational waves reinforced our understanding of gravity, defined by the century old theory of General Relativity. The fact that it stands unchallenged for such a long time is a testament to the beauty of the theory. The first direct radio image of a black hole, M87, taken by the Event Horizon Telescope collaboration in 2019 [2] reaffirmed the success of General Relativity again. Last year, in 2021, observations of radio pulsar again showed the workings of gravity and how they match what General Relativity prescribes [3]. And this year, 2022, the Event Horizon Telescope commission released a radio image of the black hole at the center of the milky way, Sagittarius A*. Within the last decade we have been able to take a glimpse at the most extreme regions of gravity. The observations made today are in accordance with the theory of General Relativity, but with our observational technology advancing at a rapid rate we might soon stumble upon something that cannot be explained. Being proven to work on scales like the solar system to incredible accuracy, General Relativity almost undoubtedly works in regions where gravity is weak[4]. If there is any place in spacetime where General Relativity is likely to fail it would be in areas of extreme gravity. The most obvious region would be near the curvature singularity of a black hole. Introducing higher order curvature terms to the Einstein-Hilbert action — the foundation of General Relativity — is the basis of Higher Derivative theories of gravity [5]. Near the curvature singularity, these higher order terms will dominate the action and thus the behavior of spacetime. The first additional order is quadratic in the curvature, the resulting theory dubbed Quadratic Gravity. The introduction of two terms quadratic in the curvature to the action have various consequences. The derivative order of the equations of motion increases, with it increasing the number of degrees of freedom. Furthermore, the quadratic terms will each introduce two mass fields to the system, a spin-two ghost mass and a spin-zero scalar mass[6]. Quadratic Gravity is an area of research that has seen increased activity in the recent decades (e.g. the Stelle group [7, 8, 9], Holdom [10], Podolsky [11], and the team of Bonanno and Silveravalle [12, 13, 14]). Currently, most research focuses on static, spherically symmetric and asymptotically flat spacetime, due to the simplifications these assumptions introduce. In the linear regime it is possible to solve the equations of motion, which can then be extended to the regime of strong-gravity [10]. The full equations of motion have analytically been investigated with the use of Frobenius analysis [11], yielding classes of solution with different scaling behaviors around either the singularity or any non-zero radius. A summary of the theoretical aspects where the research in this thesis builds upon can be found in [15]. In this thesis we continue the research of Quadratic Gravity, with the goal of finding numerical solutions to the full equations of motion in the strong-curvature regime, how they occupy the phase space, and how they could potentially be imaged. We start in section 2 with an in-depth discussion for the need of Quadratic Gravity, were we will base this on both classical arguments as well as the possibility to treat Quadratic Gravity as a theory of quantum gravity. Subsequently, section 3 covers the theory behind Quadratic Gravity, starting from the action and ending up with linearized solutions and a Frobenius analysis of the full solutions. With these theoretical results we will probe part of the phase space of solutions in section 4, where we will introduce a classification for the solutions. Furthermore, this section will include an extensive analysis of the acquired solutions, including the side-effects of using numerical tools and an attempt to extract information from the initial conditions. We will then turn towards retrieving observational quantities from the solutions in section 5. Here we will use an emission model proposed by Bambi [16, 17] to get a relation between intensity and impact parameter for our numerical solutions. These can in turn be visualized as an intensity profile — as has been done in other research [18]— resulting in images similar to the observations by the Event Horizon Telescope [2, 19]. We will then conclude with an extensive outlook where we will discuss the numerous directions future research can take. Many of the findings in this thesis will essentially follow the results in [20] and an upcoming paper that is still in the works, both of which are co-authored by the author of this thesis. Throughout the thesis we will employ the use of natural units, $c = G = 1$, unless explicitly stated.

2. THE MERITS OF QUADRATIC GRAVITY

In this thesis we will do an in-depth analysis of Quadratic Gravity. The goal of this section is to motivate this starting point. We will argue the need to explore extended theories of gravity and why Quadratic Gravity is a great starting point coming from General Relativity. With this we will briefly recap the steps used in deriving the equations of motions in General Relativity, as they will be largely the same for Quadratic Gravity, but technically less involved. Furthermore, we will discuss the use of Quadratic Gravity as a potential theory of Quantum Gravity. Here we will argue why there is a need for a quantum mechanical theory of gravity and why General Relativity alone cannot be quantized.

2.1 General Relativity

The theory of General Relativity [21], derived by Albert Einstein in the early twentieth century, has for over more than a century stood infallible as a classical description of gravity [4]. Its predictions have proven to be true in some astounding research in the last decades. The detection of gravitational waves by the LIGO collaboration [1], radio pulsar observations [3] and, almost two decades after the idea was proposed [22], the imaging of both the black hole M87 [2] and Sagittarius A* [19] by the Event Horizon Telescope are remarkable feats of science. The complexity of the theory undoubtedly holds many more secrets to be revealed in the coming years.

The core idea that sparked the theory stems from the more specific theory of Special Relativity and the thought experiments behind that theory. Postulating that the speed of light c is independent of the frame of reference — which was in accordance with the observations at that time and still is — provided a new universal constant. The constant nature of the speed of light led to a discrepancy in measurements between two relatively moving inertial frames that presumed time to be a universal feature. With Special Relativity, Einstein introduced time as a fourth dimension on top of the three spatial dimensions, altogether named spacetime. With this the concept of a spacetime metric was introduced, containing all information about distances.

A physical system can be described by an action. Through minimizing the variation of this action one can then find how the system will progress through time, with the famous Euler-Lagrange equation. In General Relativity this same idea is applied to spacetime as a whole. The theory is described by a single action that is a function of the metric. Minimizing the variation of the action with respect to the metric is then able to provide a set of equations that govern the dynamics of spacetime[23].

The action used in General Relativity is of the form

$$S = \int d^4x \sqrt{-g} \left[\frac{1}{16\pi} (R - 2\Lambda) + \mathcal{L}_M \right], \quad (1)$$

where $g_{\mu\nu}$ is the metric and g the determinant of the metric; R is the Ricci tensor, a function of the metric and its derivatives; Λ is the cosmological constant; and \mathcal{L}_M incorporates all matter fields that appear in the theory. The definition of the Ricci scalar follows through a series of other definitions.

First, since the mathematics used in this this description are tensors, we define a derivative that transforms under coordinate transformation like a tensor. The covariant derivative

$$\begin{aligned} \nabla_\sigma T_{\mu_1 \dots \mu_k}^{\nu_1 \dots \nu_l} &= \partial_\sigma T_{\mu_1 \dots \mu_k}^{\nu_1 \dots \nu_l} - \Gamma_{\sigma\mu_1}^\epsilon T_{\epsilon \dots \mu_k}^{\nu_1 \dots \nu_l} - (\dots) - \Gamma_{\sigma\mu_k}^\epsilon T_{\mu_1 \dots \epsilon}^{\nu_1 \dots \nu_l} \\ &\quad + \Gamma_{\sigma\epsilon}^{\nu_1} T_{\mu_1 \dots \mu_k}^{\epsilon \dots \nu_l} + (\dots) + \Gamma_{\sigma\epsilon}^{\nu_1} T_{\mu_1 \dots \mu_k}^{\nu_1 \dots \epsilon} \end{aligned} \quad (2)$$

does this, because the connection,

$$\Gamma_{\mu\nu}^\rho = \frac{1}{2} g^{\rho\lambda} (\partial_\mu g_{\lambda\nu} + \partial_\nu g_{\mu\lambda} - \partial_\lambda g_{\mu\nu}), \quad (3)$$

is exactly defined to make it happen. The connection is often called the Christoffel symbol (of the second order), and it is clearly not a tensor itself.

The covariant derivative is a useful tool moving vectors around a curved surface. Namely, a parallel transport of a vector V^μ along a curve $x^\mu(\tau)$ is defined as $\frac{dx^\alpha(\tau)}{d\tau} \nabla_\alpha V^\mu = 0$, the transport keeps the

covariant derivative zero. From this idea of parallel transport, the Riemann tensor can be defined as the change resulting from the parallel transport of a vector around an infinitesimally small loop,

$$[\nabla_\mu \nabla_\nu - \nabla_\nu \nabla_\mu] V^\rho = R^\rho_{\sigma\mu\nu} V^\sigma. \quad (4)$$

Expressed in as a function of the metric, we can identify

$$R^\rho_{\mu\sigma\nu} = \partial_\sigma \Gamma^\rho_{\mu\nu} - \partial_\nu \Gamma^\rho_{\mu\sigma} + \Gamma^\epsilon_{\mu\nu} \Gamma^\rho_{\sigma\epsilon} - \Gamma^\epsilon_{\mu\sigma} \Gamma^\rho_{\nu\epsilon}. \quad (5)$$

The magnitude of change due to a parallel transport carries information about the curvature of the spacetime. Curvature, in turn, describes the path of "straight" lines through the spacetime. This it what makes the Riemann tensor a great candidate for the action in General Relativity. The action, however, needs to be a scalar, thus requiring two more definitions that turn the Riemann tensor into a scalar.

First, we can contract the first and third index of the Riemann tensor to get the Ricci tensor,

$$R_{\mu\nu} = R^\rho_{\mu\rho\nu}. \quad (6)$$

Then we can take the trace of the Ricci tensor by contracting it with the metric to finally arrive at the Ricci scalar,

$$R = g^{\mu\nu} R_{\mu\nu}. \quad (7)$$

With the above definitions, we can continue the derivation of the equations of motion for the metric from the action (1). This is done by applying the variational principle to the integrand, minimizing the change of the action under a tiny perturbation in the metric,

$$H_{\mu\nu} \equiv \frac{1}{\sqrt{-g}} \frac{\delta S}{\delta g^{\mu\nu}}. \quad (8)$$

From here on it will be convenient to split the action into a pure part and a matter part, respectively,

$$S_{\text{EH}} = \frac{1}{16\pi} \int d^4x \sqrt{-g} (R - 2\Lambda) \quad (9)$$

$$S_{\text{matter}} = \int d^4x \sqrt{-g} \mathcal{L}_M. \quad (10)$$

We cannot find an explicit solution to the variation with respect to the matter Lagrangian, since its form depends on the matter that is present. Thus we define the stress-energy tensor $T_{\mu\nu}$ to contain all information on the matter distribution in the spacetime,

$$T_{\mu\nu} \equiv \frac{-2}{\sqrt{-g}} \frac{\delta S_{\text{matter}}}{\delta g^{\mu\nu}}. \quad (11)$$

We can continue with the derivation of the Einstein tensor,

$$G_{\mu\nu} \equiv \frac{1}{\sqrt{-g}} \frac{\delta S_{\text{EH}}}{\delta g^{\mu\nu}}. \quad (12)$$

, by expanding S_{EH} in $\delta g_{\mu\nu}$

$$\delta S_{\text{EH}}^{\text{pure}} \propto \int d^4x [\delta(\sqrt{-g}(R - 2\Lambda))] = \int d^4x [\delta(\sqrt{-g})(R - 2\Lambda) + \sqrt{-g}(\delta R_{\mu\nu} g^{\mu\nu} + R_{\mu\nu} \delta g^{\mu\nu})] \quad (13)$$

To evaluate this we need to investigate how a small perturbation in the metric,

$$g_{\mu\nu} \rightarrow g_{\mu\nu} + \delta g_{\mu\nu}$$

propagates to the tensorial quantities that are present in δS_{EH} . These computations, although lengthy, are quite straightforward. The complete procedure to their derivation can be found in appendix A. With these results, we can fully expand $\delta S_{\text{EH}}^{\text{pure}}$ in terms of perturbations of the inverse metric:

$$\delta S_{\text{EH}} \propto \int d^4x \left[\left(-\frac{1}{2} \sqrt{-g} g_{\mu\nu} \delta g^{\mu\nu} \right) (R - 2\Lambda) + \sqrt{-g} (R_{\mu\nu} \delta g^{\mu\nu}) + \sqrt{-g} (g^{\mu\nu}) (\nabla_\sigma (\delta \Gamma^\sigma_{\mu\nu}) - \nabla_\nu (\delta \Gamma^\sigma_{\mu\nu})) \right] \quad (14)$$

Upon closer inspection, we find that the last two terms are total derivatives. This can be made clear by manipulating the tensors,

$$\begin{aligned} \int d^4x\sqrt{-g}(g^{\mu\nu})(\nabla_\sigma(\delta\Gamma_{\mu\nu}^\sigma) - \nabla_\nu(\delta\Gamma_{\mu\lambda}^\lambda)) &= \int d^4x\sqrt{-g}(\nabla_\sigma(g^{\mu\nu}\delta\Gamma_{\mu\nu}^\sigma) - \nabla_\sigma(g^{\mu\sigma}\delta\Gamma_{\mu\lambda}^\lambda)) \\ &= \int d^4x\sqrt{-g}\nabla_\sigma(g^{\mu\nu}\delta\Gamma_{\mu\nu}^\sigma - g^{\mu\sigma}\delta\Gamma_{\mu\lambda}^\lambda) = \int d^4x\sqrt{-g}\nabla_\sigma V^\sigma \end{aligned} \quad (15)$$

The final expression here is basically a volume integral over all of spacetime of the divergence of a vector. By the divergence theorem, this is equal to the surface integral over the boundary of the volume. As our volume is all of spacetime, this boundary lies at infinity. We can set the metric perturbation at infinity to be zero. Thus this entire term vanishes.

The inverse metric can then be collected from the remaining terms in the variation of the action,

$$\delta S_{\text{EH}} \propto \int d^4x\sqrt{-g}\left(R_{\mu\nu} - \frac{1}{2}g_{\mu\nu}(R - 2\Lambda)\right)\delta g^{\mu\nu} = \int d^4x\frac{\delta S_{\text{EH}}}{\delta g^{\mu\nu}}\delta g^{\mu\nu}. \quad (16)$$

Including the stress-energy tensor (11), we have derived the equations of motions to be

$$R_{\mu\nu} - \frac{1}{2}g_{\mu\nu}R + g_{\mu\nu}\Lambda = 8\pi T_{\mu\nu} \quad (17)$$

As the action is a scalar quantity, it is invariant under any general coordinate transformation. The result is that the equations of motion should stay the same regardless of the coordinate system used to describe them. This entails the conservation law

$$\nabla^\mu H_{\mu\nu} = 0. \quad (18)$$

To conclude this derivation, we notice that in vacuum solutions, $T_{\mu\nu} = 0$, without a cosmological constant, $\Lambda = 0$, the trace of the equations of motion reveals that

$$\begin{aligned} g^{\mu\nu}\left[R_{\mu\nu} - \frac{1}{2}g_{\mu\nu}R\right] &= 0 \\ R - \frac{1}{2}4R &= 0 \\ R &= 0. \end{aligned} \quad (19)$$

Thus the equations of motion can be reduced even further to

$$R_{\mu\nu} = 0. \quad (20)$$

The Static Spherically Symmetric Solution to General Relativity

In this short intermission, we will derive the to complete set of static, spherically symmetric, and asymptotically flat solutions in General Relativity — the Schwarzschild solution [24, 25]. The procedure we will use in quadratic gravity will be very similar, though with added complexity. Having the derivation of the Schwarzschild solution will provide a reference point in this upcoming section. The Schwarzschild solution is a vacuum solution without a cosmological constant, so we will solve equation (20).

The most general spherically symmetric line element one can construct has the form [26]¹,

$$ds^2 = -h(r)dt^2 + \frac{1}{f(r)}dr^2 + r^2(d\theta^2 + \sin^2\theta d\phi^2). \quad (21)$$

¹In literature one may find slightly different definition, e.g. having $B(r) = h(r)$ and $A(r) = \frac{1}{f(r)}$.

Computing the Ricci tensor for this metric ansatz yields

$$R_{tt} = -\frac{h(r)(rf'(r) + f(r) - 1)}{r^2} \quad (22)$$

$$R_{rr} = \frac{-\frac{1}{f(r)} + \frac{rh'(r)}{h(r)} + 1}{r^2} \quad (23)$$

$$R_{\theta\theta} = \frac{1}{4}rh(r)^2(h(r)(rf'(r)h'(r) + 2f(r)(rh''(r) + h'(r))) + 2h(r)^2f'(r) - rf(r)h'(r)^2) \quad (24)$$

$$R_{\phi\phi} = \sin^2\theta R_{\theta\theta}, \quad (25)$$

all the other components vanish. Due to the conservation law (18), and the linearity between the two angular equations, we only need to solve the first two equations to find a complete solution to the system. Solving $(rf'(r) + f(r) - 1) = 0$ causes the first equation to be zero. This results in $f(r) = 1 - \frac{c_1}{r}$, which can then be substituted into the second equation to get $h(r) = c_2(1 - \frac{c_1}{r})$. Substituting these solutions into $R_{\theta\theta}$ shows that these also vanish. The coefficient c_1 is well known to be the Schwarzschild radius $r_s = 2M$, the coefficient c_2 is the freedom to redefine the time coordinate as the spacetime is static. Through normalization this is set to $c_2 = 1$. The only static, spherically symmetric metric is the Schwarzschild solution,

$$ds^2 = -\left(1 - \frac{2M}{r}\right)dt^2 + \frac{1}{1 - \frac{2M}{r}}dr^2 + r^2(d\theta^2 + \sin^2\theta d\phi^2). \quad (26)$$

This metric becomes singular at the aforementioned Schwarzschild radius. This choice of coordinates thus does not admit us to investigate the region $r < r_s$. For this reason r_s is often called the (event) horizon, as it *censors* the interior of the black hole from the outside. The asymptotic mass of the system M , thus directly determines the size of this region. It does not mean, however, that spacetime itself becomes singular at this radius, it is merely the cause of the coordinate system. The Kretschmann scalar $R^{\mu\nu\rho\sigma}R_{\mu\nu\rho\sigma}$ contains information on the curvature of the system at any point in spacetime. Its value at the Schwarzschild radius is finite, eliminating the possibility of a curvature singularity. At the center of the spacetime $r = 0$, however, there is a curvature singularity present.

In the upcoming analysis of Quadratic Gravity, we will investigate the scaling behavior of solutions that can be written as an integer power expansion. For completeness, we now determine the scaling behavior of the Schwarzschild solution, to reference to in this upcoming analysis. There are two points around which an analysis is of interest, $r = 2M$ and $r \rightarrow 0$.

The former is computed by expanding $(1 - \frac{2M}{r})$ around $r = 2M$, resulting in $\frac{(r-2M)}{2M} + \mathcal{O}((r-2M)^2)$. Thus, the leading integer power is 1 and consequently the integer scaling behavior near $r = 2M$ is thus $(r - 2M)^1$. The latter, around $r \rightarrow 0$, can be immediately deduced from $(1 - \frac{2M}{r})$. The leading integer power is -1 resulting from the scaling behavior of the term $\frac{2M}{r}$.

2.2 Extending beyond General Relativity

To date, General Relativity is in agreement with all experimental observation. This, however, is no reason not to look for new theories of gravity that go beyond that of General Relativity. It took over two hundred years for Newton's theory of gravity to be surpassed by Einstein's General Relativity. As we move through time, our technology progresses at an incredible rate. It is better technological methods that allow us to perform more precise and more ambitious observations. In the time of Newton, measurements using the Newtonian concepts of gravity were sufficient as they correctly predicted almost all observations.

We find ourselves at an exciting time in theoretical physics, with the first images of black holes appearing. This brings us to a point where we can directly observe areas of extreme gravity. It is in these areas of strong-gravity that General Relativity might not be sufficient in describing physics [4]. This may be argued as follows. The Ricci tensor in the action (17) contains information on the curvature at any point in spacetime. Most observations are done in areas of spacetime where the curvature is quite small, which is why General Relativity makes accurate predictions.

What if we add terms to the action? Keeping the idea that the terms in the action contain information on the curvature. Based on the predictability of General Relativity in areas of small curvature, the new

terms should be minuscule in these areas. The most obvious candidate would be adding terms quadratic in the curvature. Supplementing the action with these extra terms, they will be negligible in all areas of weak curvature. In areas with strong curvature, like the interior of black holes, however, these additional terms will play a significant role in determining the mechanics that govern spacetime. For this reason, Quadratic Gravity is a good candidate for extending the action of General Relativity.

With this way of thinking, we treat General Relativity not as the complete theory, but as an effective theory valid in the limit of weak curvature. This is identical to how we retrieve the Newtonian laws of physics from General Relativity in small scale experiments on earth. Quadratic Gravity is the first leading correction in a derivative expansion, but it will not necessarily be the last. Higher derivative gravity [5] is a general term for theories which include higher order terms in the curvature. Using the same argumentation we can expect cubic terms to start playing a role in extreme curvature situations. This can continue such that the action consists of an infinite sum of higher derivative terms. As one would expect, going to Quadratic Gravity severely complicates the equations of motion, which we will see in section 3. Trying to get a good picture of the implications of the additional terms in the action has been a topic in many investigations already [5, 8, 11, 14, 12], and will continue to be so for the foreseeable future.

2.3 Quantum Gravity

From the perspective of an effective field theory, Quadratic Gravity could be a natural extension to General Relativity, giving a more accurate description of the physics of black holes. This would be one reason why Quadratic Gravity is worth investigating. There is, however, another reason why a lot of research is focused on finding something beyond General Relativity. That reason being the desire for a quantum mechanical theory of gravity.

Why Quantize Gravity?

There are many reasons why we would want to find a quantum mechanical description of gravity [27]. There are phenomena in nature we currently understand very little off, like the interior of black holes and a shortage of visible matter in our galaxy indicating a need for dark matter and dark energy. Many of these unexplained phenomena take place in extreme situations; at length scales of the Planck length, at extremely high energies, and at areas of spacetime with extreme curvature. All current theories break down at these scales. A quantum theory of gravity could be the bridge to understanding the physics in these extreme cases.

Another reason to quantize gravity is not due to some unexplained phenomenon, but an intrinsic desire of finding a common description for all fundamental forces of nature. Quantum Field Theory has been able to unite three of the fundamental forces: the electromagnetic, the strong nuclear and the weak nuclear force, within one framework called the Standard Model of particle physics. The model describes the particles that constitute matter and particles that mediate the fundamental forces and how these should interact with each other. The beauty we have found in this common description sparks a desire that the fourth fundamental force, gravity, can also be described in such a way.

The last reason we will discuss has to do with a discrepancy of how time is interpreted in both Quantum Field Theory and General Relativity. In General Relativity time is just a part of spacetime, it is dynamic. In Quantum Field Theory it is not, there is no operator that describes the dynamics of time. Time is an internal feature in General Relativity but an external phenomenon to Quantum Field Theory, this is a contradiction and a quantum theory of gravity could be able to address this.

Quantizing General Relativity

There several approaches towards finding a quantum theory of gravity. Like Higher Derivative Gravity (including Quadratic Gravity), many of these approaches use General Relativity as a starting point. Examples are path-integral quantization leading to Causal Dynamical Triangulation [28] and the asymptotic safety program [29]. Quantizing General Relativity perturbatively, however, has been ruled out as an approach [30, 31]. To see exactly why this is the case, we will perform the quantization and highlight the problem we run into. We can then use the same method to quantize Quadratic Gravity and show that the problems are resolved.

We will quantize pure gravity, with the cosmological constant set to zero. Thus we start from the action $S_{\text{EH}} = \int d^4x \sqrt{-g}R$. What we will quantize is the metric itself,

$$g_{\mu\nu} = barg_{\mu\nu} + \sqrt{32\pi G}f_{\mu\nu}, \quad (27)$$

where $barg_{\mu\nu}$ is an arbitrary background metric and $f_{\mu\nu}$ is the quantized field. $f_{\mu\nu}$ has the dimension of mass, which is compensated by $\sqrt{32\pi G}$ which has an inverse mass dimension, ensuring the metric is dimensionless. In this section we will refrain from setting $G = 1$ to keep the mass dimension clearly visible. We choose the background metric to be the Minkowski metric $\eta_{\mu\nu}$.

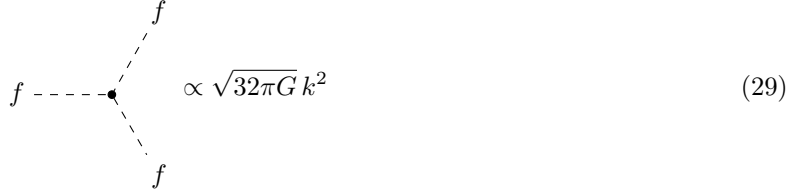
While this quantization might look similar to the perturbation we have done in deriving the equations of motion, here the quantized metric $f_{\mu\nu}$ will not necessarily be small so non-linear terms in $f_{\mu\nu}$ will appear in the action. This consequence is immediately visible in the inverse metric. As before it should be derived from the identity $\delta_\mu^\nu = g_{\mu\lambda}g^{\nu\lambda}$. Since there is no cutoff at second order, having $g^{\mu\nu} = \tilde{g}^{\mu\nu} - \sqrt{32\pi G}f^{\mu\nu}$ will introduce a non vanishing quadratic term. This can be counteracted by introducing a negating quadratic term in $g^{\mu\nu}$, with the side-effect of introducing cubic term. The process will go on indefinitely, resulting in the inverse metric containing infinite powers of $f_{\mu\nu}$.

Since this thesis' focus is classical theories, I will refrain from performing precise calculations. Instead we will roughly look at the terms that appear in the action. The Ricci tensor contains up to second order derivatives of the metric, one originating from the Christoffel connection and the other from the Riemann tensor, hence $R_{\mu\nu} \propto (\partial f_{\mu\nu})(\partial f_{\mu\nu})$. We choose to suppress the indices from here on for convenience. The Ricci scalar, that complete makes up the action, will thus contain the terms

$$\left(-\sqrt{32\pi G}f + (\sqrt{32\pi G}f)^2 - \dots \right) (\partial f)(\partial f) \propto \sqrt{32\pi G}f(\partial f)(\partial f) - (\sqrt{32\pi G}f)^2(\partial f)(\partial f) + \dots \quad (28)$$

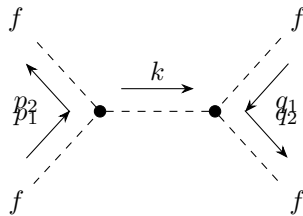
2.4 Non-Renormalizability

In quantum field theory the terms of order f^3 and higher are interpreted as possible interactions between fields. The interactions happen around vertices (points) where the fields (represented as lines) meet. The first term in equation (28), consists of three factors of f and will thus be a vertex with three lines:

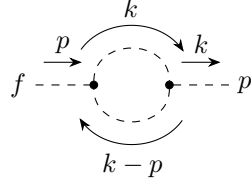


We also give an interaction strength to this vertex, equal to the factor accompanying the term in the action. In the case of the 3-point interaction we have a factor $\sqrt{32\pi G}k^2$, where k is the momentum of the field f which appears due to the two derivatives of f in this term. This is the result of a Fourier transformation, and it will play a significant role in this analysis. The other terms in the action subsequently increase the number of fields that meet at the vertex, increasing the vertex factor by $\sqrt{32\pi G}$ for each additional field. The 4-point vertex contributes similarly to the following derivation, so only using the 3-point vertex will suffice.

We can use this single vertex to create more elaborate interactions, the simplest being the one where one field is shared between two vertices.

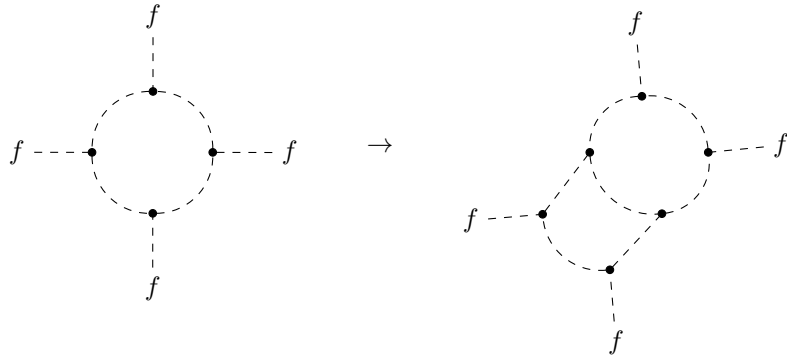


The internal field line, also known as a propagator, in the case of the field f is proportional to $\frac{1}{k^2}$. Just looking at the momentum, the entire diagram is proportional to $k^2 \times \frac{1}{k^2} \times k^2 = k^2$. The value of a diagram is used to compute the probability of such an interaction happening. In this case this is proportional to the momentum squared, meaning at higher momenta this probability diverges. Let us look at another diagram that we can make with just the vertex in (29):



This interaction has the same number of vertices as the previous one, but now has an additional propagator. The incoming and outgoing momentum are of course equal, and at each vertex we want the momentum to be conserved. Before this completely fixed the value k , but now one propagator can have any possible momentum, and the other will match the necessary momentum to ensure conservation of momenta. This thus introduces a disentangled loop momentum k , which needs to be integrated over the possible momenta. We have seen that each vertex adds a factor k^2 , while each propagator (I) adds a factor $\frac{1}{k^2}$, since we have an equal number these cancel each other. The result is that the proportionality of the interaction to the momentum is solely based on this infinite integral, which we can cut off at a momentum p_c^{UV} , $\int^{p_c^{\text{UV}}} d^4p \propto (p_c^{\text{UV}})^4$. Again, at high energies this will lead to divergences. This is bad, but not that bad as there is a way to circumvent this in quantum field theory, renormalization. If a finite number of parameters in the theory can be redefined such that the divergences disappear, then the theory is renormalizable. We note that adding a vertex to the loop, creating a new external field line, does not change this degree of divergence. Doing so simply adds one vertex and splits one propagator in two, and the contribution $I * V$ cancels.

Instead of adding a vertex to the existing loop, we can also add a propagator to create an entirely new loop



This operation has introduced two new vertices and three new propagators. The net addition is thus one extra propagator and a new loop momentum that needs to be integrated over, $\int^{p_c^{\text{UV}}} d^4k \frac{1}{k^2} \propto k^2$. Thus, the first loop has a degree of divergence $p_c^{\text{UV}4}$, and any additional loops add a factor $p_c^{\text{UV}2}$. The degree of divergence is thus dependent on the loop order as $p_c^{\text{UV}2(L+1)}$, which also agrees with our findings for if there is no loop. This result indicates that, divergences proliferate at increasing loop orders. Thus General Relativity is non-renormalizable.

The complete quantization of General Relativity is UV incomplete and thus not a Quantum Field Theory. At high energies the probabilities will irreparably diverge, indicating the break-down of the theory. There is still some merit in this quantization, however. At lower energies the theory should be able to accurately make prediction, making the quantized General Relativity an effective quantum field theory at lower energies.

Renormalizability of Quadratic Gravity

Quadratic Gravity is, opposed to General Relativity, perturbatively renormalizable. It has been known for decades, first noticed by authors [32] later formally proven [33]. A concise review is given in [6]. We can

show how adding terms quadratic to the curvature in the action modifies the above derivation in two ways. First, the quadratic nature in the curvature now results in four orders of derivatives of the metric. Using the same perturbation in equation (27), there will now be terms $\propto f(\partial f)(\partial f)(\partial f)(\partial f)$ in the action. This creates new interaction vertices that carry a factor k^4 . Looking back at the reasoning for General Relativity, this is not exactly solving any problems. If nothing else is to change, it will even create a more extreme degree of divergence.

There is, however, a second effect caused by the additional quadratic terms in the action. The increase in order of derivatives also increases the degrees of freedom in the theory. In General Relativity the degrees of freedom are visible in the matter field $f_{\mu\nu}$ as just a single massless particle, often called the graviton. In Quadratic Gravity, however, the matter field is complemented with two massive particles, one of spin-two like the graviton and one of spin-zero. These new fields are also called ghosts and their contribution is present in the propagators in the interactions. The result is that the propagator in Quadratic Gravity is proportional to $\frac{1}{k^4}$.

This is good news, since it exactly cancels the increase in order of the vertices. More importantly, we saw in General Relativity that increasing the loop order meant an additional factor of $p_c^{\text{UV}^2}$ to the degree of divergence. This was the result of the integral $\int^{p_c^{\text{UV}}} d^4 k \frac{1}{k^2}$, where the $\frac{1}{k^2}$ was due to the additional propagator being added. We now see that for Quadratic Gravity, an increase in loop order, $\int^{p_c^{\text{UV}}} d^4 k \frac{1}{k^4}$ diverges logarithmically and is independent on the momentum cutoff. Increasing the loop order thus does not lead to new divergences. After a finite number of renormalizations, these divergences will thus vanish. Quadratic Gravity is thus a renormalizable theory.

3. QUADRATIC GRAVITY

3.1 The action

In Quadratic Gravity, we extend the Einstein-Hilbert action with terms quadratic in the curvature. This does not just include R^2 , but also $R_{\mu\nu}R^{\mu\nu}$ and $R_{\rho\mu\sigma\nu}R^{\rho\mu\sigma\nu}$ as they too are distinct scalar terms that are quadratic in the curvature. Since we want to examine just the behavior of spacetime itself in quadratic gravity, we exclude any matter fields from the action, as well as setting the cosmological constant to zero. A similar analysis with a non-zero cosmological constant can be found in [34]. The quadratically extended action thus contains four total terms,

$$S = \frac{1}{16\pi} \int d^4x \sqrt{-g} [\gamma R + \zeta R_{\rho\mu\sigma\nu}R^{\rho\mu\sigma\nu} + \xi R_{\mu\nu}R^{\mu\nu} + \eta R^2].$$

Fortunately we can reduce our action by one term due to the Gauss-Bonnet theorem [35]. According to this theorem the integral $\int d^4x \sqrt{-g} [R^2 - 4R_{\mu\nu}R^{\mu\nu} + R_{\rho\mu\sigma\nu}R^{\rho\mu\sigma\nu}]$, evaluates to a trivial surface term and thus has no contribution to the dynamics of the system. We will also rewrite the remaining terms using the Weyl tensor,

$$C_{\mu\nu\rho\sigma} = R_{\mu\nu\rho\sigma} + \frac{1}{2}(g_{\mu\sigma}R_{\nu\rho} + g_{\nu\rho}R_{\mu\sigma} - g_{\mu\rho}R_{\nu\sigma} - g_{\nu\sigma}R_{\mu\rho}) + \frac{R}{6}(g_{\mu\rho}g_{\nu\sigma} - g_{\mu\sigma}g_{\nu\rho}). \quad (30)$$

Taking the square of the Weyl tensor, $C_{\mu\nu\rho\sigma}C^{\mu\nu\rho\sigma} = R_{\mu\nu\rho\sigma}R^{\mu\nu\rho\sigma} - 2R_{\mu\nu}R^{\mu\nu} + \frac{1}{3}R^2$, we see how it relates to the other scalar invariants quadratic in the curvature. With both this substitution and the Gauss-Bonnet theorem we can rewrite the action,

$$S_{\text{QG}} = \frac{1}{16\pi} \int d^4x \sqrt{-g} [\gamma R - \alpha C_{\mu\nu\rho\sigma}C^{\mu\nu\rho\sigma} + \beta R^2]. \quad (31)$$

The choice to use the Weyl tensor just convenient. Clearly, the resulting physics should not differ from an action that has the squared Ricci tensor instead (with the appropriate redefinitions of coefficients that is). However, certain features of Quadratic Gravity may be more easily recognizable with this choice. It may also simplify the resulting equations of motion, we will see this in effect once we derive the equations of motion. Likewise, choosing the operator before the Weyl term to be a minus instead of incorporating this factor into the definition of α is an arbitrary choice made out of convenience that be evident later.

3.2 The equations of motion

Deriving the equations of motion from the action (31) can again be done by varying the action with respect to a perturbation in the metric (8). The resulting equations of motion are[5],

$$H_{\mu\nu} = \gamma \left(R_{\mu\nu} - \frac{1}{2}g_{\mu\nu}R \right) - 4\alpha \left(\nabla^\rho \nabla^\sigma + \frac{1}{2}R^{\rho\sigma} \right) C_{\mu\rho\nu\sigma} + 2\beta \left(R_{\mu\nu} - \frac{1}{4}g_{\mu\nu}R - \nabla_\mu \nabla_\nu + g_{\mu\nu}\nabla^2 \right) R = 0. \quad (32)$$

These equation of motion stay the same regardless of the coordinate system used to describe them and are thus invariant under a coordinate transformation, i.e.

$$\nabla^\mu H_{\mu\nu} = 0 \quad (33)$$

is conserved.

An interesting property of these equation of motion is that its trace H^μ_μ is independent of α ,

$$H^\mu_\mu = (6\beta\nabla^2 - \gamma)R = 0, \quad (34)$$

due to the traceless nature of the Weyl tensor: $C^\rho_{\mu\rho\nu} = 0$. This is one reason one might choose including the Weyl tensor squared term in the action instead of the Ricci tensor squared. In the case $\beta = 0$ this implies that the Ricci scalar vanishes for all vacuum solutions.

3.3 Introducing a metric

Contrary to the Schwarzschild solution in General Relativity, we suspect that there will no longer be a single static spherically symmetric solution in Quadratic Gravity. Instead we aim to find the space of solutions with distinct traits. We start the investigation of this conjecture by using the most general form of the static, spherically symmetric metric (21). Plugging this ansatz into the equations of motion (32) we get four coupled differential equations. It is immediately obvious that the angular equation of motion are related by a simple factor, $H_{\phi\phi} = \sin^2 \theta H_{\theta\theta}$. Using the conservation law (33) we can express one of the remaining three equations in terms of the other, we choose $H_{\theta\theta}$ to be expressed in this way. As a result, we are left with two independent equations that fully solve the equations of motion

$$H_{tt} = 0, \quad H_{rr} = 0.$$

The complete formulas can be found in Appendix C, equation (119) and (120) respectively. A peculiar property is the differential order of these two equations. H_{tt} goes up to fourth order in $h(r)$ and third order in $f(r)$, while H_{rr} only goes to third order in $h(r)$ and second order in $f(r)$. This is by no means expected, but it does hold some valuable information. If we take the combination

$$H_{tt} - X(r)H_{rr} - Y(r)H'_{rr} = 0,$$

where we define $X(r)$ and $Y(r)$ in such a way that the $h^{(4)}(r)$ and $h^{(3)}(r)$ terms cancel, we see that the differential order of our system of equations is actually lower. The highest derivatives are now $h^{(3)}(r)$ and $f^{(3)}(r)$. Thus the system has six degrees of freedom. Any solution of this system will thus contain six free parameters. The complete form of $X(r)$ and $Y(r)$ can be found in Appendix C, equations (121) and (122) respectively.

We have seen that the system consists of two independent equations of motion. We could choose to solve $H_{tt} = 0$ and $H_{rr} = 0$ they way they are, but we are also free to consider independent linear combinations of the current equations of motion and solve these instead. We choose this approach since one specific combination has a nice property. In equation (34) we saw that the trace of the equation of motion does not depend on α and as the trace is obviously a linear combination of H_{tt} and H_{rr} this is a valid choice. The other linear combination needs to be independent of the trace, which is done by simply flipping the sign of one of the components in the trace. The equations that we will investigate are

$$H^\mu{}_\mu = 0, \quad -H^t{}_t + H^i{}_i = 0, \text{ where } i \in \{r, \theta, \phi\}. \quad (35)$$

The complexity of these equations does not admit analytic solutions. One thing we can do is checking if an ansatz is in fact a solution. This would be a terrible strategy for deriving actual solutions unique to Quadratic Gravity, but it is interesting to see how a solution to General Relativity holds up in Quadratic Gravity. The only static spherically symmetric solution to General Relativity (in vacuum) is Schwarzschild, so this is the only solution we can check for. A computer can easily do this and verify that the Schwarzschild metric is indeed a solution to Quadratic Gravity. As we will see soon, the Schwarzschild solution will become a stepping of point for investigating the different classes of solutions in Quadratic Gravity.

3.4 Deriving analytical solution classes

Since global solutions are out of reach, we need a new approach. We can use the Frobenius method to determine the admissible scaling behaviors of solutions at a point in spacetime. If the point of interest is $r = 0$, i.e. the singularity of the spacetime, we can use the general power series

$$f(r) = r^s \sum_{n=0}^{\infty} f_n r^n, \quad h(r) = r^t \sum_{n=0}^{\infty} h_n r^n \quad (36)$$

as an ansatz. The general ansatz in equation (36) will henceforth be called the Frobenius ansatz. The Frobenius method, while originally intended to find infinite series solutions to second-order ordinary differential equations, has been proven to work in related cases [11, 8]. After plugging in the ansatz into our equations of motion (35) we can expand the result into orders of r . Since the entire expansion is equal to zero, the

Analytic class $(s, t)_r$	Literature [33, 8]	Comments	Number of free parameters	Free parameters	$R_{\mu\nu\rho\sigma}R^{\mu\nu\rho\sigma}$
$(-2, 2)_0$	Stelle-(2, 2)	naked singularity	6	$h_0, f_0, f_1, f_2, h_3, f_3$	$\propto r^{-8}$
$(-1, -1)_0$	Stelle-(1, -1)	Schwarzschild-like naked singularity	4	h_0, f_0, h_3, f_3	$\propto r^{-6}$
$(0, 0)_0$	Stelle-(0, 0)	$f_0 = 1$ non-singular	3	h_0, h_2, f_2	finite
$(0, 0)_{r_0}$	Lü-(0, 0) _{r_0}	r_0 : generic	6	$\tilde{h}_0, \tilde{f}_0, \tilde{h}_1, \tilde{f}_1, \tilde{h}_2, \tilde{f}_2$	finite
$(1, 1)_{r_0}$	Lü-(1, 1) _{r_0}	r_0 : horizon	4	$r_0, \tilde{h}_0, \tilde{f}_0, \tilde{h}_1$	finite
$(1, 0)_{r_0}$	Lü-(1, 0) _{r_0}	r_0 : wormhole throat	3	$r_0, \tilde{h}_0, \tilde{f}_0$	finite

Table 1: Summary of the admissible, integer asymptotic scaling behaviors in Quadratic Gravity. In the top block are the results of the analysis at $r = 0$ (equation (36)), in the bottom block of the solutions around a non-zero r_0 (equation (37)). In the first column are the results from our Frobenius analysis, the comparison with solutions from literature can be found in the second column. The third column is dedicated to specific comments to the solutions. In the fourth and fifth comment we list the number of free parameters and which coefficients they are in the Frobenius ansatz. Finally, the last column lists the scaling behavior of the Kretschmann scalar for each solution class.

factor in front of every order of r will need to be zero. From these factors we can then deduce the values s and t are allowed to take. Furthermore, for each combination of s and t we can also put restrictions on the coefficients f_n and h_n and derive recursion relations for expressing these coefficients starting at a certain order. Here our analysis of the degrees of freedom pays off, since we know that a solution can have at most six free parameters. The parameter h_0 (or \tilde{h}_0) is peculiar in that it is a free parameter in every analytic class. This is because the assumption that our metric is static allows the time coordinate to be redefined without affecting the physics. Such a redefinition would introduce a scalar factor in the g_{tt} component of the metric. h_0 can be extracted from the expansion (36) — rescaling all the other parameters — and becomes an overall factor in the g_{tt} component. Thus, h_0 embodies the freedom to rescale the time coordinate, hence it is present in every solution class. The results of the Frobenius analysis around $r = 0$ are listed in the top half of table 1. The last column in this table details the behavior of the Kretschmann scalar $R_{\mu\nu\rho\sigma}R^{\mu\nu\rho\sigma}$ as $r \rightarrow 0$. The Kretschmann scalar is invariant under coordinate transformations and gives us insights in the nature of a singularity. In the derivation of the Schwarzschild solution in section 2.1, we found a horizon to be present at $r = 2M$. At this horizon we found a scaling behavior of $(1, 1)_{2M}$, placing it in the analytical class $(1, 1)_{r_0}$. The finding that at $r = 2M$ is not the result of a curvature singularity matches the behavior of the Kretschmann scalar for this particular class. The analysis of the Schwarzschild around $r \rightarrow 0$ gave the scaling behavior $(-1, -1)_0$, indicating that solutions of this class are Schwarzschild-like naked singularities. An important remark is that the solutions found through the Frobenius analysis is not per se the complete set of possible solutions. Solutions that cannot be analytically expressed near $r = 0$, i.e. $\ln(r)$, are not taken into account. This could possibly contain more classes of solutions.

Not all solutions will extend from asymptotic flatness at $r \rightarrow \infty$ to the central singularity at $r = 0$ of the spacetime. To investigate these cases we analyse the spacetime at a fixed point r_0 and to a Frobenius expansion around this point

$$f(r) = (r - r_0)^s \sum_{n=0}^{\infty} \tilde{f}_n (r - r_0)^n, \quad h(r) = (r - r_0)^t \sum_{n=0}^{\infty} \tilde{h}_n (r - r_0)^n. \quad (37)$$

It is also possible to include half integer powers of $r - r_0$ in this expansion. This will lead to additional solutions, but these will not be considered in the scope of this research. The results of the Frobenius analysis around r_0 can be seen in the bottom half of table 1.

3.5 Linearizing the equations of motion

The Frobenius analysis gives an analytical tool to gain insights into possible classes of solutions, each characterized by their scaling behavior near the point of expansion. Another analytical way of approaching the equations of motion is through linearization. The goal of linearization is to closely approximate a solution to the full equations of motion (35). To tackle this challenge, it will be useful divide the entire spacetime, from $r = 0$ to $r \rightarrow \infty$, into regions and per region look at what we already know. At $r = 0$ is a curvature singularity, then for radius close to the singularity, including for instance the event horizon in the case of a Schwarzschild black hole, the effects of the curvature are strong, we call this the strong field regime. Now we skip all the way towards $r \rightarrow \infty$, here the effects of the central singularity vanish asymptotically. We are left with the unperturbed flat spacetime of Special Relativity, the Minkowsky spacetime $\eta_{\mu\nu} = \text{diag}(-1, 1, 1, 1)$. This desired feature of spacetime being flat asymptotically far away from any perturbations, is called asymptotic flatness. We can use these two extremes to identify an interesting third regime in between the two. Since the spacetime is asymptotically flat, the metric (or expansion of the metric in r) can only depend on inverse powers of r . In the strong regime, where r is small, all terms in this expansion will contribute significantly to the value of the metric. As we move away from the singularity and r increases the higher order terms start vanishing, until at a certain point the linear term is the only significantly contributing term left. In this linear regime (or weak field regime) we will look for a solution to the linearized equations of motion. The following analysis has been done in the literature and will follow past procedures closely, see [33, 12].

To start of we need to linearize the equations of motion (35). The metric in the weak field regime should differ from Minkowski by only a linear perturbation:

$$g_{\mu\nu} = \eta_{\mu\nu} + \epsilon f_{\mu\nu} = \begin{pmatrix} -1 & 0 & 0 & 0 \\ 0 & 1 & 0 & 0 \\ 0 & 0 & 1 & 0 \\ 0 & 0 & 0 & 1 \end{pmatrix} + \epsilon \begin{pmatrix} -V(r) & 0 & 0 & 0 \\ 0 & -W(r) & 0 & 0 \\ 0 & 0 & 0 & 0 \\ 0 & 0 & 0 & 0 \end{pmatrix}$$

This is equivalent with the substitution

$$f(r) \rightarrow 1 + \epsilon W(r) \quad h(r) \rightarrow 1 + \epsilon V(r).$$

Substituting this in the equations of motion and keeping only terms linear in ϵ gives us the linearized equations of motion

$$\begin{aligned} H_{\text{lin}}^{\mu}_{\mu} &= -\frac{24\beta W}{r^4} + \frac{24\beta W'}{r^3} - \frac{12\beta W''}{r^2} + \frac{2\gamma W}{r^2} - \frac{24\beta V^{(3)}}{r} + \frac{2\gamma V'}{r} \\ &\quad - \frac{12\beta W^{(3)}}{r} + \frac{2\gamma W'}{r} - 6\beta V^{(4)} + \gamma V'' \\ -H_{\text{lin}}^t + H_{\text{lin}}^i &= \frac{8\alpha W}{3r^4} - \frac{8\beta W}{r^4} - \frac{8\alpha W'}{3r^3} + \frac{8\beta W'}{r^3} + \frac{4\alpha W''}{3r^2} - \frac{4\beta W''}{r^2} - \frac{16\alpha V^{(3)}}{3r} - \frac{8\beta V^{(3)}}{r} \\ &\quad + \frac{2\gamma V'(r)}{r} + \frac{4\alpha W^{(3)}}{3r} - \frac{4\beta W^{(3)}}{r} - \frac{4}{3}\alpha V^{(4)} - 2\beta V^{(4)} + \gamma V'' \end{aligned} \tag{38}$$

Defining $Y(r) = \frac{(rW(r))'}{r^2}$, we can represent these equations more neatly

$$\begin{aligned} H_{\text{lin}}^{\mu}_{\mu} &= -6\beta (\nabla^2 \nabla^2 V(r) + 2\nabla^2 Y(r)) + \gamma (\nabla^2 V(r) + 2Y(r)) = 0 \\ -H_{\text{lin}}^t + H_{\text{lin}}^i &= -4(\beta - \frac{\alpha}{3}) \nabla^2 Y(r) - 2(\beta + \frac{2\alpha}{3}) \nabla^2 \nabla^2 V(r) + \gamma \nabla^2 V(r) = 0, \end{aligned}$$

where ∇^2 is the Laplace operator.

Solutions to the linear equations

These linear equations can be solved using Fourier-methods. Introducing the masses corresponding to the massive spin-two and spin-zero degrees of freedom,

$$m_2 = \sqrt{\frac{\gamma}{2\alpha}} \quad m_0 = \sqrt{\frac{\gamma}{6\beta}}, \tag{39}$$

the linear solutions then take the general form

$$f(r) = 1 - \frac{2M}{r} + S_2^+ \frac{e^{m_2 r}}{r} (1 - m_2 r) + S_2^- \frac{e^{-m_2 r}}{r} (1 + m_2 r) - S_0^+ \frac{e^{m_0 r}}{r} (1 - m_0 r) - S_0^- \frac{e^{-m_0 r}}{r} (1 + m_0 r)$$

$$h(r) = 1 + C_T - \frac{2M}{r} + 2S_2^+ \frac{e^{m_2 r}}{r} + 2S_2^- \frac{e^{-m_2 r}}{r} + S_0^+ \frac{e^{m_0 r}}{r} + S_0^- \frac{e^{-m_0 r}}{r}.$$

Analyzing this solution provides plentiful information about the underlying theory. The number of free parameters that are present in the solution, $M, C_T, S_2^+, S_2^-, S_0^+$ and S_0^- , is indeed equal to six. We can immediately reduce this number by half by imposing two conditions. First, we obviously notice that C_T is a constant term present in $h(r)$, thus embodying the freedom to rescale the time parameter. We canonically normalize our time parameter and use this freedom to set $C_T = 0$. Second, we desire the spacetime to be asymptotically flat, so $f(r) = h(r) = 1$ as $r \rightarrow \infty$. Since the parameters S_2^+ and S_0^+ are associated with exponentially growing modes, we set $S_2^+ = S_0^+ = 0$. The linear solutions specific to our spacetime have thus reduced to,

$$f(r) = 1 - \frac{2M}{r} + S_2^- \frac{e^{-m_2 r}}{r} (1 + m_2 r) - S_0^- \frac{e^{-m_0 r}}{r} (1 + m_0 r) \quad (40)$$

$$h(r) = 1 - \frac{2M}{r} + 2S_2^- \frac{e^{-m_2 r}}{r} + S_0^- \frac{e^{-m_0 r}}{r}. \quad (41)$$

Thus we are left with 3 free parameters for any finite masses m_0 and m_2 .

The masses of the spin-two mode (corresponding to the $C_{\mu\rho\nu\sigma}C^{\mu\rho\nu\sigma}$ -term) and spin-zero mode (corresponding to the R^2 -term) are inversely proportional to their respective coefficients, see equation (39). If the terms where to vanish, i.e., setting α and β to zero, the masses become infinite. We can see in the linear solution that infinite masses result in the vanishing of the exponential terms and only $f(r) = h(r) = 1 - \frac{2M}{r}$ is left. We expect this, as for α and β vanishing the action becomes that of General Relativity. The Schwarzschild solution is the only static spherically symmetric solution to the full equations of motion, and since it also solves the linearized Einstein equations, we also expect it to be the only solution of the linearized equations of motion in General Relativity. We can also quickly investigate what would happen if we choose a negative value for α or β . The respective mass would evaluate to a complex number that would be present in an exponent in the solution. The result would be an oscillating term that by their nature can never become zero in the asymptotic limit. This case is thus ruled out and $\alpha \geq 0, \beta \geq 0$. It is for this reason that we defined the action to have an extra minus factor in front of the α term, it is convenient that either coefficient can never be negative.

Of the three leftover parameters, we can thus identify M as the same central mass that is known from the Schwarzschild solution in General Relativity. The remaining two parameters S_2^- and S_0^- are the new parameters of linearized quadratic gravity. They encode the contribution of the massive spin-two and spin-zero modes to the geometry. If they are both zero, the linear solutions return to the Schwarzschild solution. Although the resulting linear solutions for $S_2^- = S_0^- = 0$ are the same as when we have $\alpha = \beta = 0$, they are very distinct cases that should not be confused. The former is a unique solution within Quadratic Gravity that behaves identical to the Schwarzschild solution in General Relativity. The latter is the result of the limit where Quadratic Gravity resorts to General Relativity, where we expect that Schwarzschild is the only viable solution.

4. NUMERICAL ANALYSIS OF THE EQUATIONS OF MOTION

We now stray away from trying to solve the equation in an analytical way and look at numerical solutions. Using a numerical integrator the computer can use the full equations we provide, plug in numerical values for all unknowns except for the highest derivatives, compute what these highest derivatives should be for the equation to be valid, and then finally use these found values to update all lower derivatives. A computer can do this entire procedure extremely fast and as often as we would like, although there are downsides.

Firstly, computers can only store decimal values to a certain level of precision, so a numerical solution will always contain a small error. While an error to a single computation is often minute, the problem is that in a numerical integrator—where many successive calculations are done—each error is propagated to all subsequent computations. The error will thus grow exponentially as a function of the number of iterations. The consequence of this is that a numerical solution can only reasonably cover a small part of the complete solution. Edge cases, where even the tiniest change results in a different outcome, are often unpredictable and misrepresent the true underlying solution.

Secondly, we need to provide a set of initial conditions to computer. Of course, any set of initial conditions will lead to a numerical solution, but generating one at random will most likely not have any actual physical meaning. Ideally, we need the solution to give us the initial conditions that generate a solution. This is quite the paradox and thus quite impossible. What we can do, however, is get a really close approximation to an actual solution and use that to generate reasonable initial conditions. Then we hope that the tiny divergence from the true solution does not influence the behavior of the numerical integrator too much, so that we end up with a close to real solution.

The solutions (40) to the linearized equations of motion (38) can be used to represent the solution in the weak-field regime and the asymptotically flat region. We choose an initial point r_i in this regime to generate the initial conditions for the numeric integration. The numerical integrator extends the solution from r_i inward until it hits a singularity. We can freely choose the radius r_i at which we switch from linear solution to the numerical integrator. In this choice we inherently make a trade off. Ideally we choose r_i very large so we are deep in the weak-field regime where the weak field representation extremely precise. However, as discussed previously, this requires the integrator to run for longer and increases the error in the computation. We can only circumvent this by choosing a smaller r_i where the weak-field approximation is less precise.

Besides the free parameters in the solution, we also need to choose the parameters of the action in a certain way. We fix $\gamma = 1$, this is sets the overall scale. If we impose that quadratic action (31) becomes the action of General Relativity as $\alpha, \beta \rightarrow 0$, we thus have $\gamma = \frac{c^4}{G}$, but since we have $c = G = 1$, this becomes one. For α and β we look at how they relate to the mass of their respective fields. From the definitions (39) and the above choice for γ we see that in the case $\alpha = \frac{1}{2}$ and $\beta = \frac{1}{6}$ both masses equal one in Planck units. We deem this a good starting point for choosing these parameters, as both mass fields are at "equal strength". Contrary to γ we will not fix them at these value and instead investigate the space of solutions by varying these masses.

There are a total of six variable parameters in the numerical integration, $M, S_2^-, S_0^-, \alpha, \beta$, and r_i . One might believe this is again a consequence of having a maximum of six free parameters in the theory. However, this is not the case and a mere coincidence. There is indeed a maximum number of six free parameters within the theory, however α and β are parameters that define the theory. Changing them changes the theory, and thus they are on a different level than the other parameters. On the other side, the parameter r_i is an artifact of using numerical methods to find the solution. It does not contain any meaning in the context of the theory or the solutions, but we need to introduce it to be able to perform the numerical analysis.

4.1 Solution classes

In the probing of the phase space (coming up in the next section, figure 5 and 5) we will distinguish three classes of solutions, one of which can be further reduced into three subclasses. Added to these three classes, we also have the trivial class containing only the Schwarzschild solution² and the group for the few numerically

²We have discussed before that for $S_2^- = S_0^- = 0$ the solution to the linearized equations of motion reduces to the Schwarzschild equation, which is also a unique solution to the complete equations of motion. The numerical integrator will,

Solution class	γ	α	β	M	S_2^-	S_0^-	r_i	Example Fig	Intensity Fig
Type I	1	1/2	1/6	10	1/200	-1/15	35	1a	
Type Ia	1	1/2	1/6	10	1/200	-1/150	35	2 blue	10a
Type Ib	1	1/2	1/6	10	1/200	-1/15	35	2 orange	10a
Type Ic	1	1/2	1/6	10	1/200	-2/3	35	2 green	10b
Type II	1	1/2	1/6	10	2	1/100	35	1b	10c
Type III	1	1/2	1/6	10	1/200	1/15	35	1c	10a

Table 2: Initial conditions for the numerical integration procedure generating the representative geometry for each class. All figures presented in our work build on the corresponding solutions.

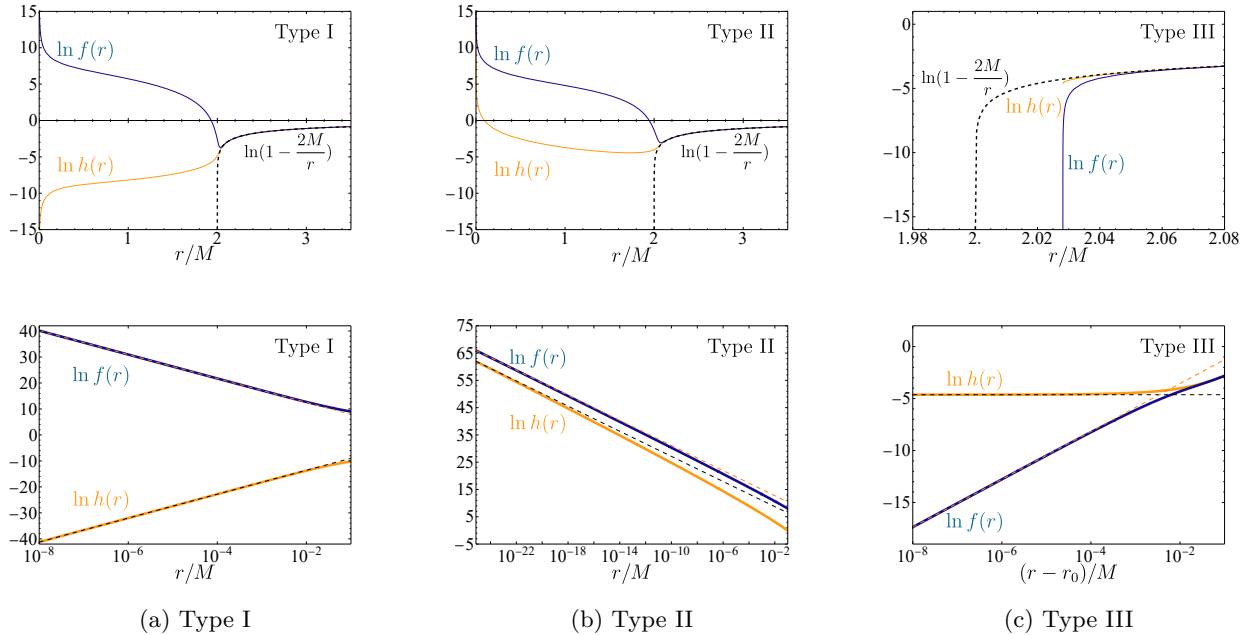


Figure 1: Illustration of the topologically distinct global solutions in quadratic gravity. The solutions are obtained from solving (35) numerically with initial conditions given in Table 2. The top line displays the radial dependence of $\ln f$ (blue curve) and $\ln h$ (orange curve) for the solutions of (a) Type I, (b) Type II, and (c) Type III. The Schwarzschild solution with $M = 10$ and an event horizon at $r/M = 2$, is superimposed as the dashed line. The lower row shows the scaling behavior of the solutions as $r \rightarrow 0$ (Type I and Type II) as well as for $r - r_0 \rightarrow 0$ (Type III) in a double logarithmic presentation. The scaling behaviors are $(s, t)_0 = (-2, 2)_0$ for Type I, $(s, t)_0 = (-1, -1)_0$ for Type II, and $(s, t)_{r_0} = (1, 0)_{r_0}$ for Type III. Graphs of the respective power law are superimposed as dashed lines (black for h and orange for f). This links the asymptotically flat, global solutions to the classification of local scaling behaviors identified in Table 1.

inconclusive solutions³.

Type I: For these solutions the numerical integration is reliable until $r \approx 0$. For $r \gtrsim 2M$, the functions $h(r)$ and $f(r)$ essentially follow the Schwarzschild solution, before starting to deviate substantially for $r \lesssim 2M$.

however, due to tiny errors stray from this Schwarzschild solution and thus put the result into a different group of solutions. Hence, we have to manually assign these cases to be the Schwarzschild solution.

³Numerically inconclusive solutions show up at borders between two solution classes. We expect that these cases are borderline cases in which the error is of the same or greater order than the values in the integration. These solutions are thus completely governed by the error and hence named inconclusive.

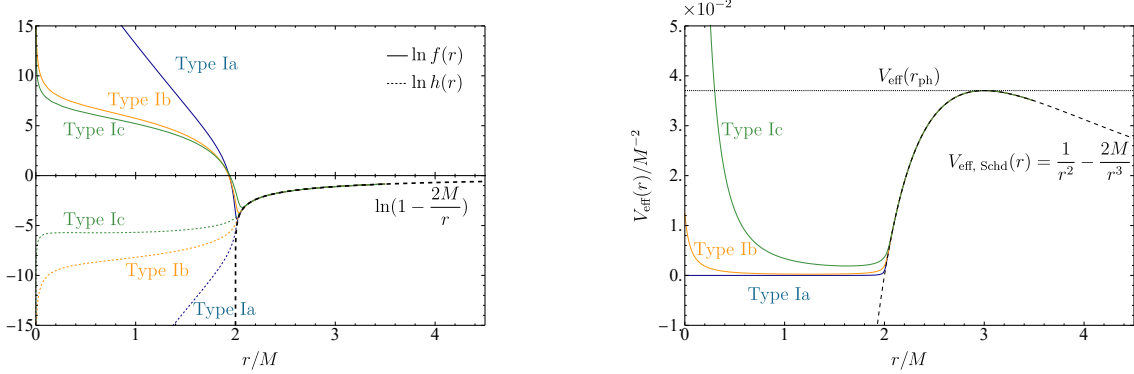


Figure 2: Refinement of the Type-I classification. The solutions arise from the initial conditions given in Table 2 for objects of mass $M = 10$. The left panel displays $\ln f$ (top, solid) and $\ln h$ (bottom, dashed), showing the typical behavior of the Type I solutions given in Fig. 1a. The refinement follows from considering $V_{\text{eff}} = h(r)/r^2$, shown in the right panel. For Type Ia solutions V_{eff} decreases monotonically for $r < 3M$. For Type Ib solutions the potential has a stable minimum and $V_{\text{eff}}(0) < V_{\text{eff}}(3M)$. The characteristic feature for Type Ic solutions is that $\infty > V_{\text{eff}}(0) > V_{\text{eff}}(3M)$.

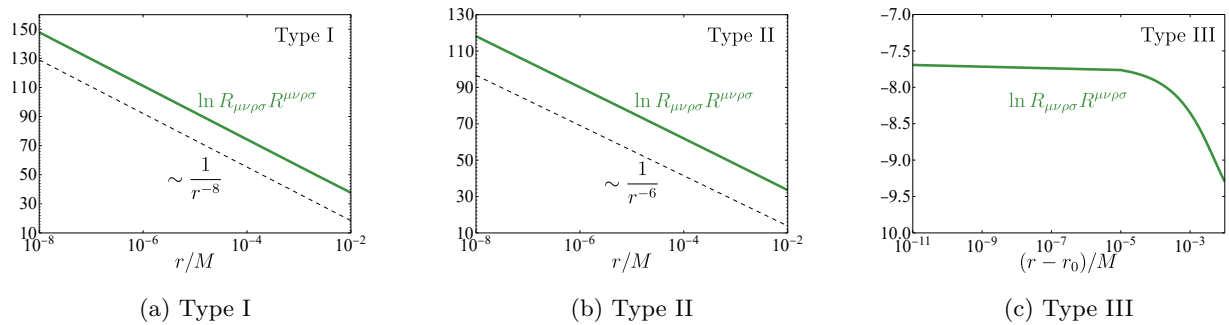


Figure 3: An illustration of the behavior of the Kretschmann scalar $R_{\mu\nu\rho\sigma}R^{\mu\nu\rho\sigma}$ (green curve), for the solutions of (a) Type I, (b) Type II, and (c) Type III using the same initial conditions as the example solutions in figure 1. The scaling behavior as $r \rightarrow 0$ (for Type I and Type II) is portrayed with a dashed line and is $\sim \frac{1}{r^8}$ and $\sim \frac{1}{r^6}$ respectively. For solutions of Type III ($r - r_0 \rightarrow 0$) the scaling is finite.

At $r \ll 1$, the scaling behavior of $h(r)$ and $f(r)$ follows the local expansion with $(s, t)_0 = (-2, 2)_0$, i.e.,

$$f(r) \sim f_0 r^{-2}, \quad h(r) \sim h_0 r^2, \quad (42)$$

where \sim indicates that the relations hold asymptotically. This constitutes the defining criterion for geometries of Type I. The characteristic example for these solutions is shown in Fig. 1a.

Furthermore, we can also plot the behavior of the Kretschmann scalar close to the termination point. This is done for the same initial conditions in Fig. 3a. As expected from the Frobenius analysis in Tab. 1, the scaling for a $(-2, 2)_0$ -solution indeed goes as r^{-8} .

The effective radial potential governing the motion of light-rays within the geometry is given by $V_{\text{eff}}(r) = h(r)/r^2$ (see equation (79)). The scaling properties (42) then imply that $V_{\text{eff}}|_{r=0}$ is finite. This suggests a refined classification based on the value h_0 , controlling the height of V_{eff} at $r = 0$. From the perspective of observations, it is natural to discriminate the three subclasses displayed in Figure 2:

Type Ia In this case the value of h_0 is small in the sense that $V_{\text{eff}}(r)$ decreases monotonically for $r < 3M$ while staying positive. In the phase space plot, Fig. 5, Type Ia is indicated by pink color.

Type Ib Here, $V_{\text{eff}}|_{r=0} \leq V_{\text{eff}}|_{r=r_{\text{ph}}=3M}$. In contrast to Type Ia, the effective potential has a stable minimum between $r = 0$ and $r = 3M$. In the phase space plot, Figure 5, Type Ib is indicated by red color.

Type Ic By definition, these geometries obey $V_{\text{eff}}|_{r=0} > V_{\text{eff}}|_{r=r_{\text{ph}}=3M}$. The effective potential has a stable minimum between $r = 0$ and $r = 3M$. In the phase space plot, Figure 5, Type Ic is indicated by orange color.

Type II: Similarly to Type I, the numerical integration of this class of solutions is reliable up to very small values $r \approx 0$. Again the functions h and f follow the Schwarzschild solution for $r > 2M$ and deviate for $r \leq 2M$. The defining property of this class is its characteristic scaling behavior as $r \rightarrow 0$,

$$f(r) \sim f_0 r^{-1}, \quad h(r) \sim h_0 r^{-1}. \quad (43)$$

Thus they belong to the analytic class $(-1, -1)_0$ which describes naked singularities [8]. An example solution is illustrated in Figure 1b. The Kretschmann scalar goes as $\sim r^{-6}$ as can be seen in figure 3b. In the phase space plot, Figure 5, Type II is indicated by yellow color.

Type III: The numerical integration for this solution class terminates at a radius $r_{\text{term}} > 2M$, at radii slightly larger than the position of the would-be horizon of a Schwarzschild black hole with equal asymptotic mass. Close to the termination point

$$f(r) \sim f_0 (r - r_{\text{term}}), \quad h(r) \sim h_0, \quad (44)$$

so that these geometries fall into the analytic class $(1, 0)_{r_0}$. An example Type III solution is illustrated in Fig. 1c. From the plot of the Kretschmann scalar in figure 3c we can confirm it stays finite, meaning the termination point is not due to a spacetime singularity. Instead, this corresponds to wormhole solutions [8]. In the phase space plot, Fig. 5, Type III is indicated by black color.

A summary of each solution class is presented in table 3.

4.2 Probing the Phase Space

For our systematical scan the phase space of solutions, we choose three variables to vary. Since this research is among the first to investigate the phase space, we opt for a qualitative investigation of a small part of the space over a quantitative scan over a large part⁴. The remaining variables will have to be fixed.

First of all, we look at solutions with asymptotic mass M given by 10 Planck masses. With this choice we assume that varying the mass — while changing the scale — will not affect the physics. We choose this

⁴In the upcoming investigation we evaluate the phase space at 6500 points. It is reasonable to assume that a single computation takes ten seconds. The entire computation can run on a single processing core, meaning that in a multi-threaded setup, many computations can run in parallel. Scanning broader sections of the phase space will be a plausible and interesting step, but is not done in this work.

Solution class	Analytic class	Color in Fig. 5	Defining characteristic
Type S	$(1, 1)_{r_0}$	purple	Schwarzschild geometry (unique)
Type Ia	$(-2, 2)_0$	pink	naked singularity, no stable photon orbit below $r = 2M$
Type Ib	$(-2, 2)_0$	red	naked singularity, stable photon orbit below $r = 2M$
Type Ic	$(-2, 2)_0$	orange	naked singularity, partially screened by a reflective barrier
Type II	$(-1, -1)_0$	yellow	naked singularity, fully screened by a reflective barrier
Type III	$(1, 0)_{r_0}$	black	wormhole throat at finite $r_{\text{term}} > 2M$
None	None	white	inconclusive initial conditions due to numerical instability

Table 3: Mapping numeric solution classes to analytic classes. Characteristic properties of the asymptotically flat vacuum solutions in quadratic gravity are presented, see Fig. 5.

value as it will be about an order of magnitude greater than the newly introduced masses m_2 and m_0 . A very similar analysis as recently emerged in [14], in which the mass is taken as one of the variables in a three-dimensional phase space. Second of all, we choose to set $\alpha = \frac{1}{2}$. By varying just one of the theory's parameters we lose the ability to compare the quadratic contributions in the action (31) to the linear one, i.e. $\frac{\gamma}{\beta}$ is fixed⁵. Will can, however, still investigate the effect the ratio of $\frac{\alpha}{\beta}$ has on the phase space by varying just β . Since there is still little known on the shape of the phase space, we can expect limiting ourselves to just varying β will still result in valuable information and it is thus a worthy trade-off. Lastly, we choose to fix $r_i = 3.5M = 35$. Varying the radius where we switch from linear solution to numerical will undoubtedly change some solutions, and we will briefly discuss this in an upcoming section 4.3. For constructing the phase space, we can consider it best to fix it at one value for all solutions to be calculated so the numerical error in every solution is of the exact same origin. The value of $r_i = 35$ is chosen as it is at a reasonable distance from the event horizon of the Schwarzschild solution at $r_s = 2M = 20$, and the numerical integrator is able to reach solutions that extend towards nearly zero.

This leaves the parameters β , S_2^- , and S_0^- as our variables. We then constructed a three-dimensional phase space, here β takes the nine values: $(\frac{1}{3}, \frac{1}{4}, \frac{1}{5}, \frac{1}{6}, \frac{13}{84}, \frac{1}{7}, \frac{1}{8}, \frac{1}{10}, \frac{1}{18})$ and both S_2^- and S_0^- take the twenty-seven values: $(\pm 10, \pm 5, \pm 2, \pm 1, \pm 0.5, \pm 0.2, \pm 0.1, \pm 0.05, \pm 0.02, \pm 0.01, \pm 0.005, \pm 0.002, \pm 0.001, 0)$. The resulting phase space is represented in nine two-dimensional grids in figure 5. In this grid we separate the results of the numerical integration into solution classes based on the behavior of the solutions near the termination point of the integration. Each solution class is represented by its own color, for a total of seven solution classes. We will now discuss the characteristics of each solution class to their full extend.

Properties of the Phase Space

We now highlight the interesting features of the phase space (figure 5). As mentioned before, the Schwarzschild solution can only be obtained by setting $S_2^- = S_0^- = 0$ and is the only solution with an event horizon. The other classes are either naked singularities (Type I and Type II), or wormhole solutions (Type III). In General Relativity, Birkhoff's theorem states that the only static, spherically symmetric solution is the Schwarzschild solution. In Quadratic Gravity we have seen that this is no longer the case, but with this unique property of having an event horizon we can modify Birkhoff's theorem for Quadratic Gravity: The Schwarzschild solution and the Stelle black hole solution [7] are the only asymptotically flat, static, and spherically symmetric solution in Quadratic Gravity that is compatible with the cosmic censorship hypothesis. The Stelle black hole solution is a second solution branch with an event horizon found in [7]. This branch only exists for $M \leq 0.438\sqrt{2\alpha\gamma}$, hence it does not appear in this work and is mentioned here solely for completeness.

We know that for $\beta = \frac{1}{6}$, the spin-two and spin-zero masses are equal. From the resulting phase space for this value of β , we see that there is a symmetry between S_2^- and S_0^- . This leads us to believe that

⁵ $\frac{\gamma}{\beta}$ will of course not be fixed, but we argue that for a complete analysis on how the quadratic terms relate to the linear one we would want to have both terms free.

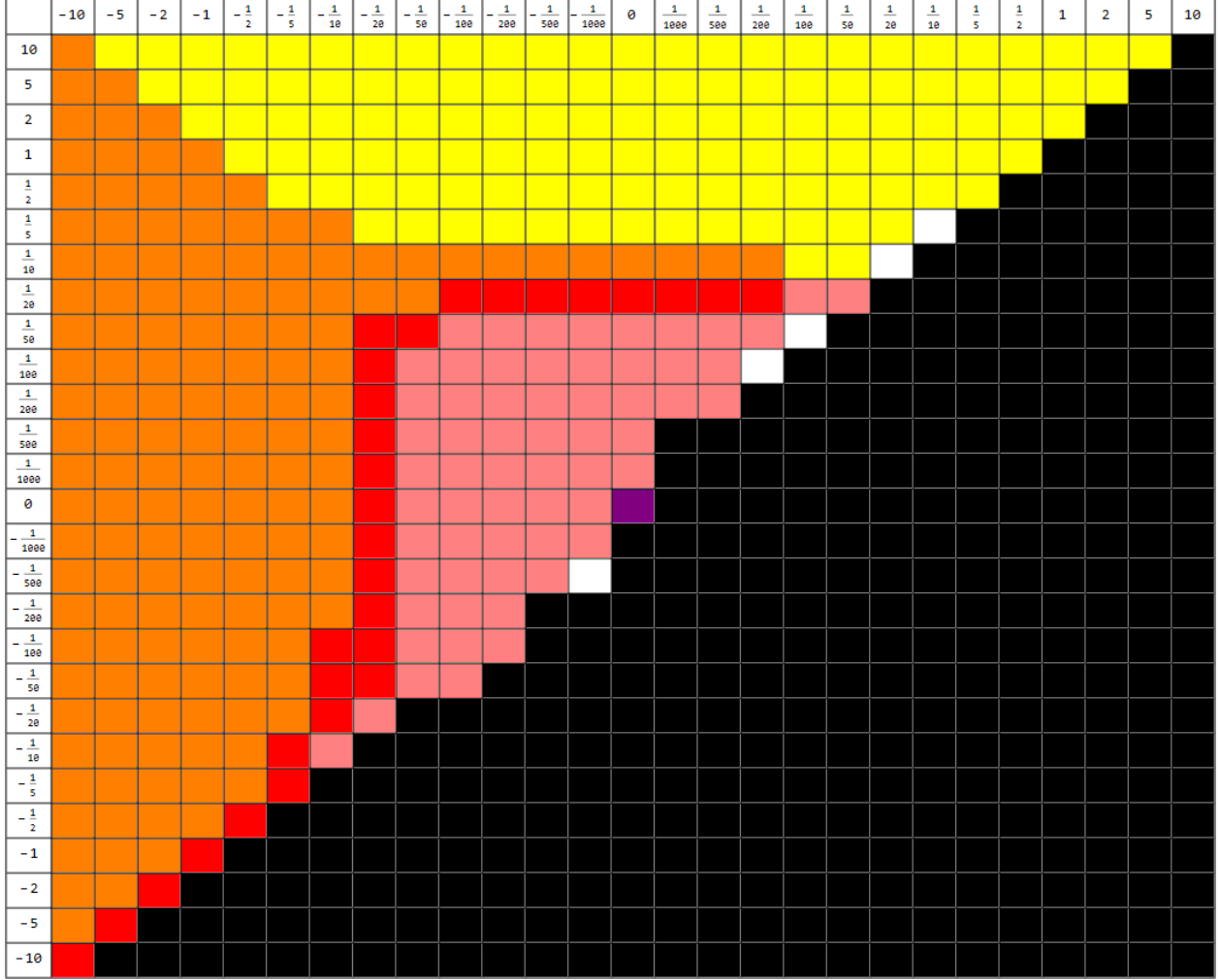


Figure 4: A slice of the phase space. The values for S_0^- and S_2^- are $(\pm 10, \pm 5, \pm 2, \pm 1, \pm 0.5, \pm 0.2, \pm 0.1, \pm 0.05, \pm 0.02, \pm 0.01, \pm 0.005, \pm 0.002, \pm 0.001, 0)$. Throughout the figures the remaining parameters are fixed at $\gamma = 1$, $M = 10$, $r_i = 35$, $\alpha = 1/2$, and $\beta = 1/6$. Color coding distinguishes the numeric solution classes as indicated in Table 3.

both quadratic terms are of equal strength here. If β increases, m_0 decreases and the dampening of the corresponding Yukawa terms decreases. It can also be interpreted as the $C_{\mu\nu\rho\sigma}C^{\mu\nu\rho\sigma}$ -term in the action being overshadowed by the R^2 -term. We can see this in effect, as the phase space becomes less dependent on S_2^- . For large β it the phase space gets divided in two sections, one with Type III solutions, one with Type II solutions. Somewhere in the region $\frac{1}{5} < \beta < \frac{1}{4}$ there should be a value at which the phase space changes more radically, as seen in figure 5 where the region of Type III solution complete shifts between $\beta = \frac{1}{5}$ and $\beta = \frac{1}{4}$. This exact point was not found in the scope of this research. If we decrease β towards zero, we see the opposite happening. The $C_{\mu\nu\rho\sigma}C^{\mu\nu\rho\sigma}$ -term becomes dominant and the solutions become less dependent on S_0^- . We again see a divide in the phase space, with Type Ib solutions for $S_2^- > 0$ and Type III solutions for $S_2^- \leq 0$.

Divergence from integer scaling

Before we conclude this section, a remark to the way we have performed our classification is in order. We have assumed that every solution falls into one of the possible solution classes found from the Frobenius analysis. It is to be expected, however, that not every solution will be as good of a match to the integer

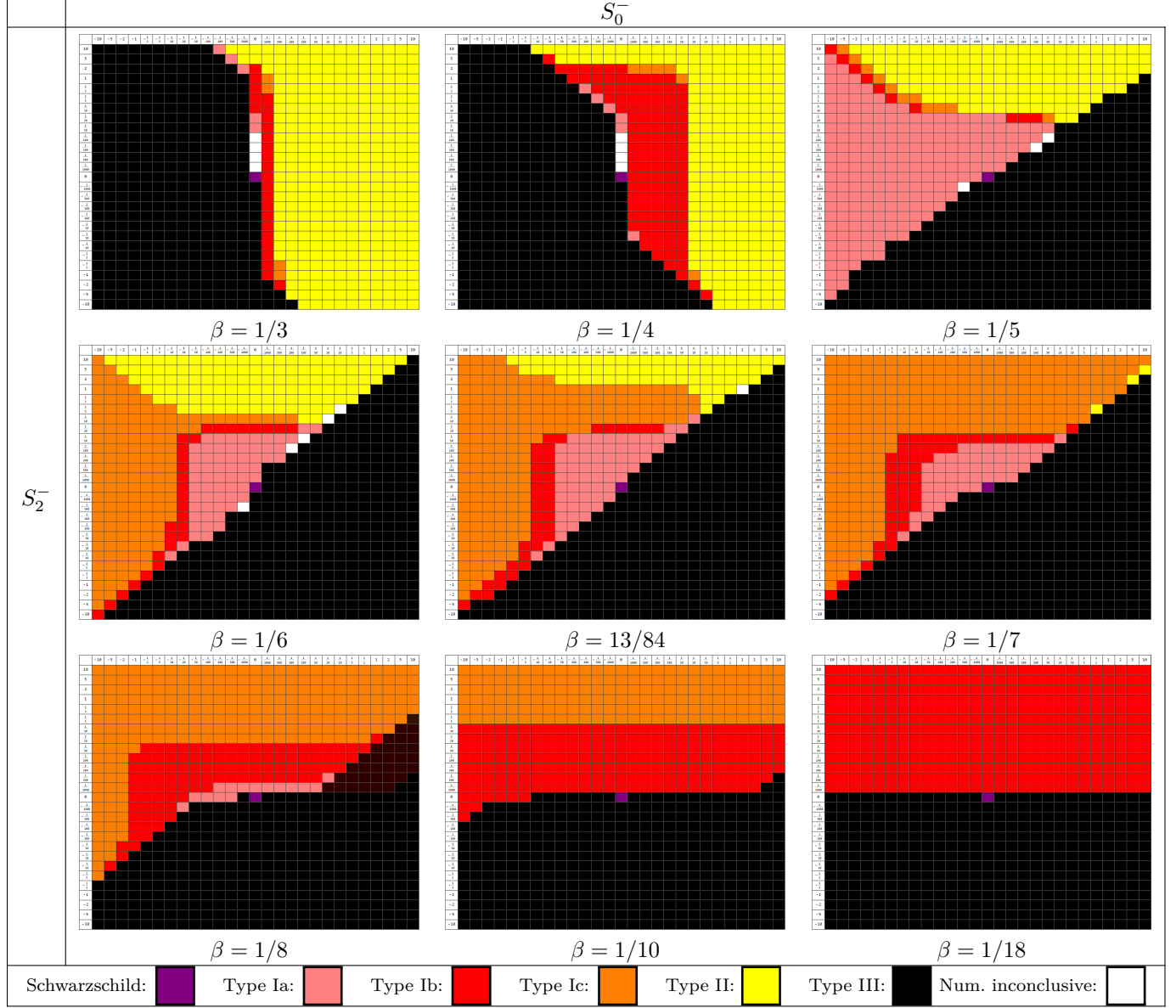


Figure 5: A number of representative β -slices through the phase space. The values for S_0^- and S_2^- are $(\pm 10, \pm 5, \pm 2, \pm 1, \pm 0.5, \pm 0.2, \pm 0.1, \pm 0.05, \pm 0.02, \pm 0.01, \pm 0.005, \pm 0.002, \pm 0.001, 0)$. Throughout the figures the remaining parameters are fixed at $\gamma = 1$, $M = 10$, $r_i = 35$, and $\alpha = 1/2$. Color coding distinguishes the numeric solution classes as indicated in Table 3.

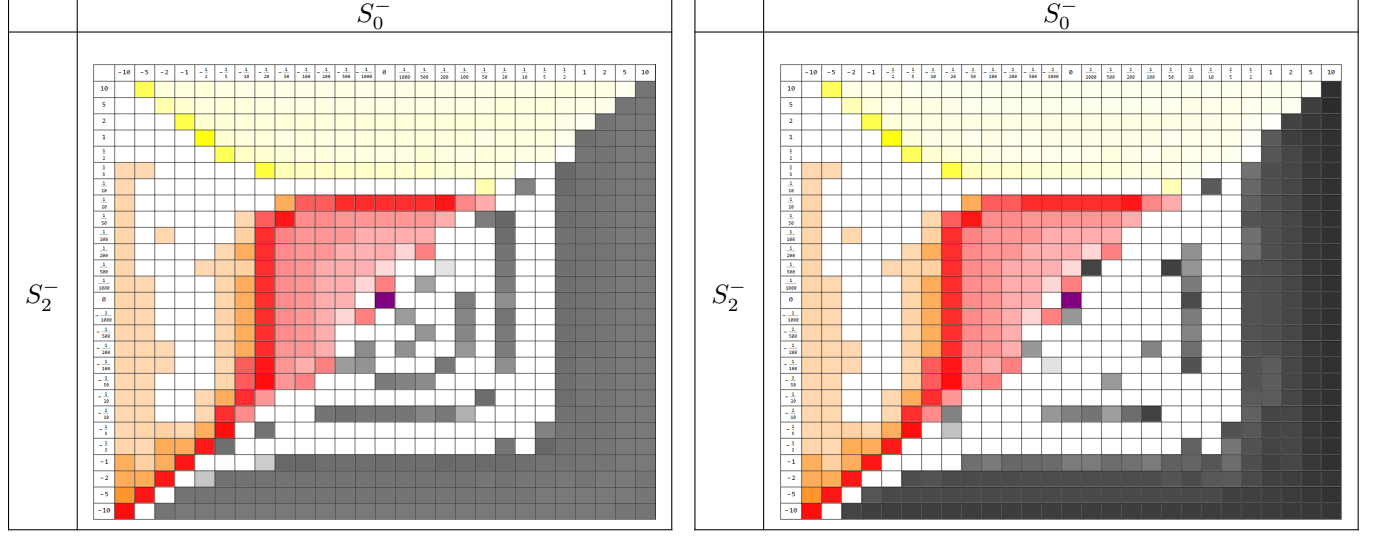
scaling values. Similar research [36] has put restrictions on how much a solution can deviate from integer values. This warrants a deeper look into these deviations for our phase space.

We indeed see some deviation in the scaling behavior in figure 6. In the construction of this image we have taken the β -slice of the phase space where $\beta = 1/6$. For each solution we use the points closest the termination point to perform a non-linear fit of both $\ln f(r)$ and $\ln h(r)$ to respectively

$$\ln f_{\text{fit}}(r) = C_f + s_{\text{fit}} \ln(r) \quad (45)$$

$$\ln h_{\text{fit}}(r) = C_h + t_{\text{fit}} \ln(r). \quad (46)$$

With the use of a fitting algorithm this yielded a s_{fit} and a t_{fit} for each solution. These were then compared with the integer values from the theory. In figure 6 we used the absolute value of the difference between the


 (a) $f - \text{fit}$

 (b) $h - \text{fit}$

Figure 6: A β -slice of the phase space ($\beta = 1/6$, see figure 5) where opacity has been used to indicate the accuracy of a logarithmic fit. For each cell the solution was fitted near the termination point using equation (45), the results were subjected to equation (47) to determine the opacity of the according cell in the image. The left image applied the fitting to $f(r)$, using the sensitivities: $\sigma_{\text{Type I}} = 3 \times 10^{13}$, $\sigma_{\text{Type II}} = 50$, and $\sigma_{\text{Type III}} = 15$. The right image applied the fitting to $h(r)$, using the sensitivities: $\sigma_{\text{Type I}} = 3 \times 10^{13}$, $\sigma_{\text{Type II}} = 18$, and $\sigma_{\text{Type III}} = 5 \times 10^{10}$.

two to set the opacity of the accompanying cell. The opacity was calculated with the equation

$$\text{Opacity} = 1 - \sigma |i_{\text{fit}} - i_{\text{theory}}| \quad \text{where } i = s, t, \quad (47)$$

where we have introduced σ as a sensitivity parameter. This parameter is necessary to make the deviations actually visible in the figure and its values gives good insights to the order of magnitude of the deviation for the solution class. The higher the sensitivity, the smaller the deviations.

The value for σ heavily depends on the class of solutions we look at. For all Type I solutions we have set $\sigma = 2 \times 10^{13}$ for both the f and h fit. This means that these solutions all follow integer scaling to great precision. Taking the average of all fits we indeed see that the deviations is only from the eleventh decimal place and onwards. Furthermore, as both fits (f and h) can use the same sensitivity and show up almost indistinguishable on the plot, we can say with high accuracy that the classification of these points as Type I is correct.

Continuing to Type II solution class, we use $\sigma = 50$ for the f -fit and $\sigma = 18$ for the h -fit. Compared to the Type I solution class, the solutions in this class follow the integer scaling much less precisely. The average fit deviates roughly 2.5% from what is expected from the theory. There is also a small disparity between the f -fit and h -fit, where the latter has more cases with greater divergence. Still, considering all other numerical errors present due to the integration, we accept this deviation and classify all these solutions as Type II solutions.

Finally, the Type III solution class is distinguished by the stark contrast between the f -fit and the h -fit. For the former we have set $\sigma = 15$ and we have an average fitting parameter of $s_{\text{fit,average}} = 0.91$, almost 10% from the theoretical value. While for the latter we have $\sigma = 5 \times 10^{10}$ and the average is of order $t_{\text{fit,average}} \sim 10^{-11}$. There is a huge contrast in the precision of the two fits, with the h -fit being extremely accurate, while the f -fit seems to fail, as in some extreme cases the fit deviates up to 40%. Still, this can be explained to some extend. We have seen that Type III solutions follow the Schwarzschild solution only until very close to the termination point, where $f(r)$ suddenly decreases very rapidly to zero. When $f(r)$ is (almost) zero the equations of motion become singular, resulting in its termination. This rapid change in $f(r)$ will cause a stark increase in the derivatives of $f(r)$. We can thus expect that the process of diverging

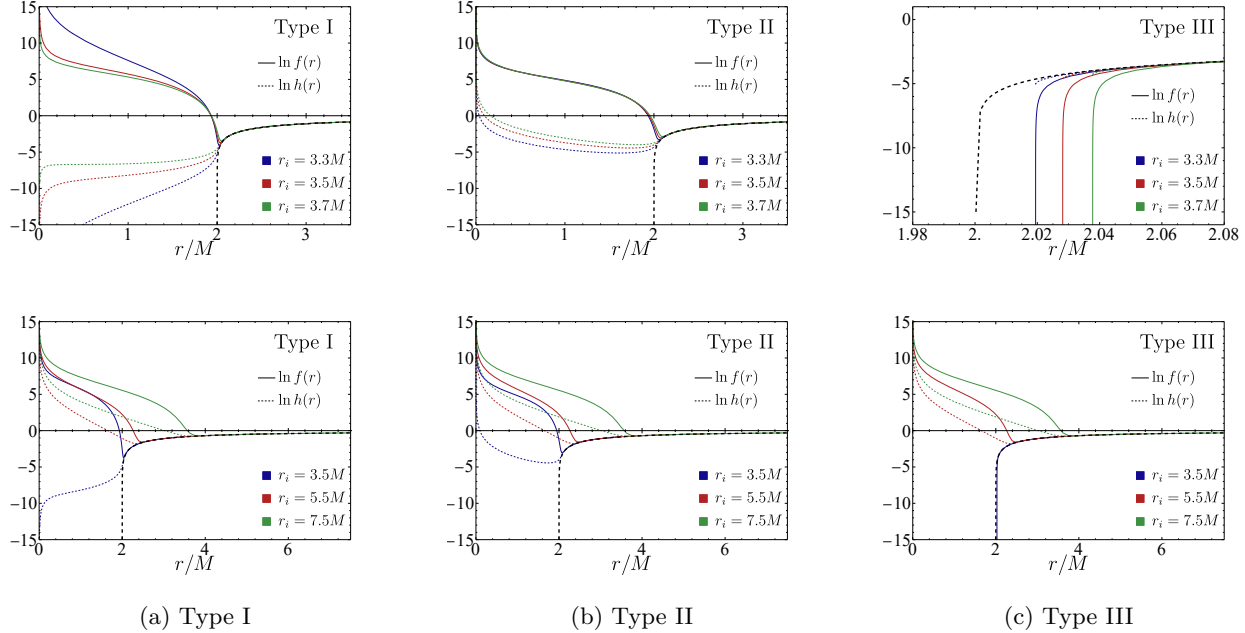


Figure 7: A comparison between numerical solutions with differing initial radii r_i . The same initial conditions listed in table 2 are used except for r_i , which is set at the values $(33, 35, 37)$ in the top row and values $(35, 55, 75)$ in the bottom row. Colors are used to distinguish the solutions on their initial radius. $\ln h(r)$ is plotted with a line dashing, while $\ln f(r)$ is plotted as a straight line. On all graphs, the Schwarzschild behavior $\ln(1 - \frac{2M}{r})$ is plotted as a thick dashed black line.

from Schwarzschild to reaching the termination point happens within just a few integration steps, that each deal with enormous values, prone to greater numerical error. Thus a fit through these points will be far less accurate. The function $h(r)$, on the other hand, becomes constant. This can be approached far more smoothly from the Schwarzschild solution, resulting in a near perfect fit.

Based on the accuracy of the h -fit and on the near perfect half of the phase space these solutions occupy, we have assumed that all these solutions can correctly be categorized as Type III. With the extreme situation of the f -fit near the termination point and the not too large average error of 10%, we do not believe to make a great error in this assumption.

4.3 Sensitivity on the Initial Radius r_i

In the above analysis we have kept r_i fixed for reasons argued for in the beginning of this section. Still, there is some merit in knowing how solutions will change once we vary this parameter. If the numerical integration is highly sensitive to small changes in r_i , the analysis will be less accurate as a whole. This would be especially true if the high sensitivity alters the phase space picture. We will change r_i on two scales in order to get a basic understanding of its effects on the numeric calculations. First, we will do a narrow variation, probing the same solutions as in figure 1, but with an initial radius of $r_i = 33$, $r_i = 35$ and $r_i = 37$. This gives us reasonable insights in how the phase space could change if we had chosen a slightly different r_i . Then, we will do a greater variation on these solutions, with $r_i = 35$, $r_i = 55$, and $r_i = 75$, as it will be interesting to see when the integration breaks down.

In the top row of figure 7 we see the result of applying a slight variation to the initial radius. The solutions seem to break away from Schwarzschild sooner for larger values of r_i . We also notice that, while the exact values of the solution do significantly change, their general shape does not. The resulting limit at the termination point seem unaffected as a result. Based on these result we argue that the phase space in figure 5 is robust against small variations of the initial radius. This gives us more confidence in the result,

since it is less likely to be the results of some sort of numerical noise from the numerical integrator.

Applying greater variations to the initial conditions, however, does significantly impact the resulting solutions, as can be seen in the bottom row of figure 7. All three solutions, that previously showed different behaviors, now take the form a Type II solution, even Type III solutions, that previously terminated at $r > 2M$, are now able to diverge from Schwarzschild and reach the singularity. Numerical precision inevitably plays a role here, and it can easily be demonstrated. From equation (40) we see that the initial radius influences the initial conditions in an exponent. This exponents then is used as to generate a slight deviation from the Schwarzschild solution, which for our chosen variable is roughly of order 1. A computer's machine precision is only finite, so when it had to add two values of different orders of magnitude e^0 and e^{-55} , much of the precision of the smaller value will be lost⁶. Due to the limited precision, the numerical errors that emerge have a similar size of the deviation itself. As a result the initial conditions are quickly overshadowed by the error, which accordingly determines the shape of the solution. For this reason, the provided parameters S_2^- and S_0^- no longer matter, as they won't be able to make a difference in whether or not the error takes over. We can see this in the figure, as the solutions for $r_i = 5.5M$ and $r_i = 7.5M$ look identical (and are identical to a great number of digits) across the three different classes. This illustrates the window of r_i in which we can actually get sensible results.

It is interesting though, that a numerical error pushes the integration to a Type II solution. There is no easy way to distinguish what causes a solution to end up as a certain solution class, something we will cover in an upcoming section. While this is mere speculation, it could be that there is a consistency in the way the error propagates in the numerical integration. The consistency of the error might always trigger the right conditions for the solution to become a Type II solution. Though there might also be cases where another solution family becomes the home to numerical errors.

4.4 Initial Conditions and Stress Energy Tensor

The equations of motion in General Relativity (17) can in principle be solved by any spacetime by choosing a matter configuration whose stress-energy tensor exactly equates to the Einstein tensor. The question is whether the underlying matter configuration is actually realistic. Consequently, it is possible that a spacetime that requires the presence of (exotic) matter in General Relativity, appears as a vacuum solution in Quadratic Gravity. An example of this are wormholes. In General Relativity wormholes can only form in the presence of an exotic matter source, i.e., a matter configuration that violates the weak energy condition. In the solutions we found and in existing literature [37], however, wormholes are the result of vacuum solutions in Quadratic Gravity and Higher Derivative Gravity. Thus, to get a better understanding of the contributions arising from the higher-derivatives terms, we treat Quadratic Gravity as General Relativity with an "effective" stress-energy tensor encoding the contributions from C^2 and R^2 terms. Doing this will give us a stress-energy configuration for General Relativity that would precisely mimic the contributions attributed to Quadratic Gravity. We can easily compute the values the stress-energy tensor by either computing the terms linear or quadratic in the curvature.

From the equations of motion for General Relativity (17), we can express

$$T_{\mu\nu} = \frac{1}{8\pi} \left(R_{\mu\nu} - \frac{1}{2} g_{\mu\nu} R \right). \quad (48)$$

Similarly, we could derive equations for the effective stress-energy tensor by equation it to the quadratic terms,

$$T_{\mu\nu} = \frac{1}{8\pi} \left[4\alpha \left(\nabla^\rho \nabla^\sigma + \frac{1}{2} R^{\rho\sigma} \right) C_{\mu\rho\nu\sigma} - 2\beta \left(R_{\mu\nu} - \frac{1}{4} g_{\mu\nu} R - \nabla_\mu \nabla_\nu + g_{\mu\nu} \nabla^2 \right) R \right]. \quad (49)$$

For all vacuum solutions to Quadratic Gravity, these yield the same results. Since the complexity of the former equations is lower, the preference goes to them.

Using the static, spherically symmetric metric ansatz (21), the effective stress-energy tensor can be

⁶As an example, say our precision is ten decimal places. If we want to add the values 1 and $1.1234567890 \times 10^{-10}$, the result is 1.0000000001. Most of the information of the smaller value has been lost.

expressed in terms of the metric functions $f(r)$ and $h(r)$,

$$T_{tt} = \frac{1}{8\pi} \left(-\frac{h(r)(rf'(r) + f(r) - 1)}{r^2} \right), \quad (50)$$

$$T_{rr} = \frac{1}{8\pi} \left(\frac{-\frac{1}{f(r)} + \frac{rh'(r)}{h(r)} + 1}{r^2} \right), \quad (51)$$

$$T_{\theta\theta} = \frac{1}{8\pi} \left(\frac{r(h(r)(rf'(r)h'(r) + 2f(r)(rh''(r) + h'(r))) + 2h(r)^2f'(r) - rf(r)h'(r)^2)}{4h(r)^2} \right), \quad (52)$$

$$T_{\phi\phi} = \sin^2 \theta T_{\theta\theta}. \quad (53)$$

We evaluate the right-hand side equations (48) using the Quadratic Gravity solutions and check if the stress-energy tensor induced by the deviations for General Relativity are compatible with energy conditions familiar from standard matter. Concretely, we implement the following energy conditions:

WEC The Weak Energy Condition (WEC) states that $T_{\mu\nu}t^\mu t^\nu \geq 0$, where t^μ is an arbitrary timelike vector. To check this condition we first need to construct an arbitrary timelike vector: $t^\mu = (1, a, 0, 0)$, normalized such that $t^\mu t_\mu < 0$. We are able to set the last two entries to zero due to the spherical symmetry of the spacetime. The normalization condition for the metric (21) thus is

$$t^\mu t_\mu = -h(r) + \frac{a^2}{f(r)} < 0 \quad \leftrightarrow \quad a^2 < f(r)h(r). \quad (54)$$

The WEC consequently reads

$$T_{tt} + a^2 T_{rr} \geq 0 \quad \leftrightarrow \quad a^2 \geq -\frac{T_{tt}}{T_{rr}}. \quad (55)$$

As the WEC needs to hold for every possible timelike vector, it is more straightforward to see if there is a timelike vector breaking the WEC. With the use of a computer it can quickly be determined if a system of equalities can be solved.

NEC The same procedure can be done for the Null Energy Condition (NEC) $T_{\mu\nu}l^\mu l^\nu \geq 0$, where l^μ is a like-light vector. The procedure is identical to the WEC except for the normalization condition changing to $l^\mu l_\mu = 0$. Using the same ansatz for $l^\mu = (1, a, 0, 0)$, this gives an expression for a^2

$$l^\mu l_\mu = -h(r) + \frac{a^2}{f(r)} = 0 \quad \leftrightarrow \quad a^2 = f(r)h(r). \quad (56)$$

As a result the NEC $T_{tt} + a^2 T_{rr} \geq 0$ is independent of a :

$$f(r)h(r) + \frac{T_{tt}}{T_{rr}} \geq 0, \quad (57)$$

SEC The Strong Energy Condition (SEC) is $T_{\mu\nu}t^\mu t^\nu - \frac{1}{2}T_\rho^\rho t^\sigma t_\sigma \geq 0$, where t^μ is again a timelike vector with the normalization (54). For the specific stress-energy tensor (48), the SEC evaluates to

$$T_{tt} + a^2 T_{rr} - \frac{1}{2} \left(-\frac{T_{tt}}{h(r)} + f(r)T_{rr} + 2\frac{T_{\theta\theta}}{r^2} \right) \left(-h(r) + \frac{a^2}{f(r)} \right) \geq 0 \quad (58)$$

We proceed by analyzing the content of these equations. Checking these conditions for an actual solution results in an interesting find. For the probed points in the phase space for $\beta = \frac{1}{6}$, a point either fails all conditions or passes all conditions. Furthermore, most solutions are either true at every radius, or false at every radius. This suggests that the initial conditions might hold considerable information on the class of the resulting solution.

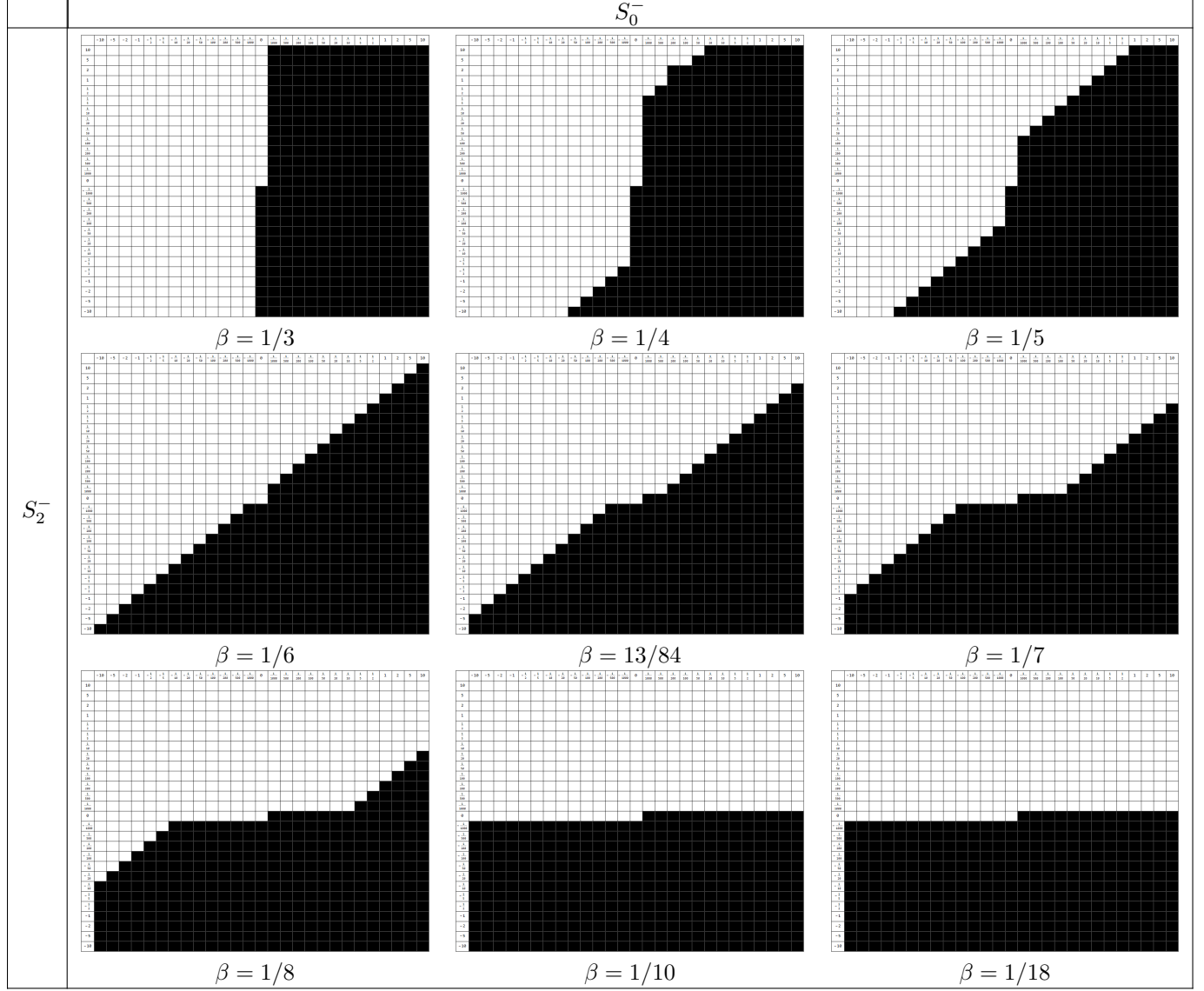


Figure 8: A number of representative β -slices through the phase space. The values for S_0^- and S_2^- are $(\pm 10, \pm 5, \pm 2, \pm 1, \pm 0.5, \pm 0.2, \pm 0.1, \pm 0.05, \pm 0.02, \pm 0.01, \pm 0.005, \pm 0.002, \pm 0.001, 0)$. Throughout the figures the remaining parameters are fixed at $\gamma = 1$, $M = 10$, $r_i = 35$, and $\alpha = 1/2$. Color coding distinguishes the energy condition violation, black cells violate the conditions while the white cells do not.

For every point probed in the phase space in figure 5 we can check whether the stress-energy tensor at the associated initial conditions pass the energy conditions. The result is shown in figure 8. It is immediately obvious that the energy conditions split the phase space in half, one side where the solutions satisfy the SEC and one where they fail. While the dividing border seems to go through the origin, the Schwarzschild solution at the origin is strictly part of the successful half, since $T_{\mu\nu} = 0$ by construction. Furthermore, the separation in the phase space rotates as β changes. From a large β , where the border is vertical ($S_0^- = 0$), through $\beta = 1/6$, where the border is diagonal ($S_0^- = S_2^-$), to small β , where the border is horizontal ($S_2^- = 0$). This rotating behavior was also present in the phase space of solutions, although it is not completely similar.

Comparing the solution classes with the energy condition test we find something peculiar. For $\beta = 1/6$ the region where the energy conditions fail in figure 8 almost perfectly align with the region occupied by Type III solutions in figure 5. This similarity continues as β decreases, both regions rotating at the same rate. A correlation between Type III solutions and failing energy conditions is not unexpected. As previously

discussed, Type III solutions are considered to be wormholes that mimic black holes on the outside. We mentioned in the introduction of this section that in General Relativity wormhole solutions need exotic matter.

For large values of β , however, the correlation breaks down. Type III wormhole solutions seem to follow from initial conditions that pass the energy conditions and the other way around. The energy conditions at the initial conditions do not have any predictive power over what the resulting solution will be. It is most likely that there is no physical relation between the energy conditions at the initial conditions and the resulting solution. Since there is no reason to believe that Quadratic Gravity should abide by the conditions postulated for matter configuration in General Relativity, this result is to be expected. The similarity for small β is most likely a coincidence. The smaller values α and β take, the closer Quadratic Gravity resembled General Relativity, which could be an explanation for this coincidence.

Comparison to a Perfect Fluid

We can make a brief comparison of the individual components of the stress-energy tensor with the energy and momentum density defined for a perfect fluid. We do not want these components to depend on the choice of metric, thus we look at scalar quantities. The stress-energy tensor of a perfect fluid is defined as,

$$T_{\mu\nu} = (\rho(r) + p(r))U_\mu U_\nu + p(r)g_{\mu\nu}, \quad (59)$$

where $\rho(r)$ is the energy density, $p(r)$ the pressure density, and U^μ the four-velocity of the perfect fluid. The trace is independent on frame of reference and point in spacetime,

$$T^\mu_\mu = -\rho(r) + 3p(r). \quad (60)$$

We limit this investigation in the linear regime, where we have analytic solutions, it can, however, also work with numerical solutions. We substitute the initial conditions (40) for the functions $f(r)$ and $h(r)$ and keep the terms linear in the parameters S_2^- and S_0^- ,

$$T_t^t = \frac{S_0^- m_0 e^{-m_0 r} - S_2^- m_2 e^{-m_2 r}}{r^2} \quad (61)$$

$$T_r^r = \frac{S_0^- m_0 (r - 2M) e^{-m_0 r} - S_2^- m_2 (1 - 4m_2 M + 2m_2 r) e^{-m_2 r}}{r^2(r - 2M)} \quad (62)$$

$$T_\theta^\theta = \frac{S_0^- m_0^2 e^{-m_0 r}}{2r} \quad (63)$$

$$+ \frac{S_2^- (2M^2 m_2 (4m_2 r + 1) - M (8m_2^2 r^2 + 3m_2 r + 1) + r (2m_2^2 r^2 + m_2 r + 1)) e^{-m_2 r}}{2r^2(r - 2M)^2} \quad (64)$$

$$T_\phi^\phi = T_\theta^\theta = p(r). \quad (65)$$

We observe that $T_r^r \propto (r - 2M)^{-1}$ and $T_\theta^\theta \propto (r - 2M)^{-2}$. Furthermore, at $r = 2M$ the term with S_0^- vanishes in both T_r^r and T_θ^θ , while the S_2^- does not. Consequently, for non-zero S_2^- the values of T_r^r and T_θ^θ will increase drastically at the horizon. This explains why we can have General Relativity at large distances and modifications to the geometry close to the horizon.

In an arbitrary reference frame, $U^\mu = (A(r), A(r)\sqrt{f(r)(h(r) - \frac{1}{A(r)^2})}, 0, 0)$ where $A(r)$ is an arbitrary function of r (conforming to the definition $U^\mu U_\mu = -1$ of the four-velocity). Since we assume the spacetime to be spherically symmetric, we set the angular components to zero without loss of generality. We now express the individual components of the stress-energy tensor like before,

$$T_t^t = -A(r)^2 h(r) \rho(r) + (1 - A(r)^2 h(r)) p(r) \quad (66)$$

$$T_r^r = (A(r)^2 h(r) - 1) \rho(r) + (A(r)^2 h(r)) p(r) \quad (67)$$

$$T_\phi^\phi = T_\theta^\theta = p(r). \quad (68)$$

Note that for the choice $A(r) = \frac{1}{\sqrt{h(r)}}$, the spatial components of U^μ vanish and we find the rest frame of the fluid. Because of the choice of an arbitrary reference frame, it is now possible to conduct a comparison

between the sets of equations (61) and (66). This reveals — within a given theory where α and β are fixed — three equations with three unknown scalar functions $\rho(r)$, $p(r)$, and $A(r)$. Since $A(r)$ is an arbitrary function related to the reference frame, it cannot influence the physics that govern the geometry of the spacetime. This becomes apparent when we take the sum of both sets of equations (which is simply the trace of the stress-energy tensor) and the final equation of the set as our two equations that can be solved for $\rho(r)$ and $p(r)$. These two equations are independent of $A(r)$ and give to linear order,

$$\rho(r) = \frac{S_0^- m_0 (m_0 r + 4) e^{-m_0 r}}{2r^2} \quad (69)$$

$$+ \frac{S_2^- (2M^2 m_2 (4m_2 r + 13) - M (8m_2^2 r^2 + 27m_2 r + 5) + r (2m_2^2 r^2 + 7m_2 r + 3)) e^{-m_2 r}}{2r^2(r - 2M)^2}, \quad (70)$$

$$p(r) = \frac{S_0^- m_0^2 e^{-m_0 r}}{2r} \quad (71)$$

$$+ \frac{S_2^- (2M^2 m_2 (4m_2 r + 1) - M (8m_2^2 r^2 + 3m_2 r + 1) + r (2m_2^2 r^2 + m_2 r + 1)) e^{-m_2 r}}{2r^2(r - 2M)^2}. \quad (72)$$

$$(73)$$

As a result, equating these two sets of equations reveals a mapping that expresses the scalar functions in terms of the free parameters of the theory, as well as the variable r . With this mapping, existing knowledge on the energy and momentum density can be applied to better understanding the parameters introduced in Quadratic Gravity.

We can subject the scalar functions above to the energy conditions for a perfect fluid. The WEC and NEC give $\rho(r) + p(r) \geq 0$ and $\rho(r) \geq 0$, and the SEC adds the condition that $\rho(r) + 3p(r) \geq 0$. This gives a simple way to test the energy conditions in the weak-field at different radii r . In figure 8 we observed that at values of $\beta > 1/6$ there was no correlation between the solution class and if the energy conditions at the initial radius r_i are satisfied.

Plotting the energy conditions of the scalar functions above as a function of r , reveals that there the satisfaction of the energy conditions can indeed change as the radius decreases. In figure 9 we visualize the energy conditions for a Type II solution that violates the energy conditions at $r = r_i$. We see a sharp peak around $r = 2M$ where the energy conditions are all satisfied. This is a clear indication that it is difficult to analytically determine the solution type from the behavior in the weak-field regime. As discussed previously, due to factors of $(r - 2M)^{-1}$ in the analytical expression of the scalar fields, the effective stress-energy tensor becomes singular. The linear approximation and weak-field theory clearly breaks down at this point and the spacetime becomes highly non-linear. It is thus unlikely that a set of analytical expressions derived in the weak-field regime can predict the class of a solution.

This feature is intrinsic to Quadratic Gravity and thus present no matter the scale of the system. So while the effects of the perturbation are limited in the weak-field regime, the non-linearity is not. Consequently, for any system in nature the perturbations are negligible (and will be shown in the upcoming section), but a modification of the geometry itself close to the horizon is unavoidable. Thus, any observation that wishes to test the theory of Quadratic Gravity would need to probe the interior of the black hole through physical phenomena caused by the modification of the geometry. It is thus impossible for an observation of the exterior of a black hole to rule out Quadratic Gravity as theory.

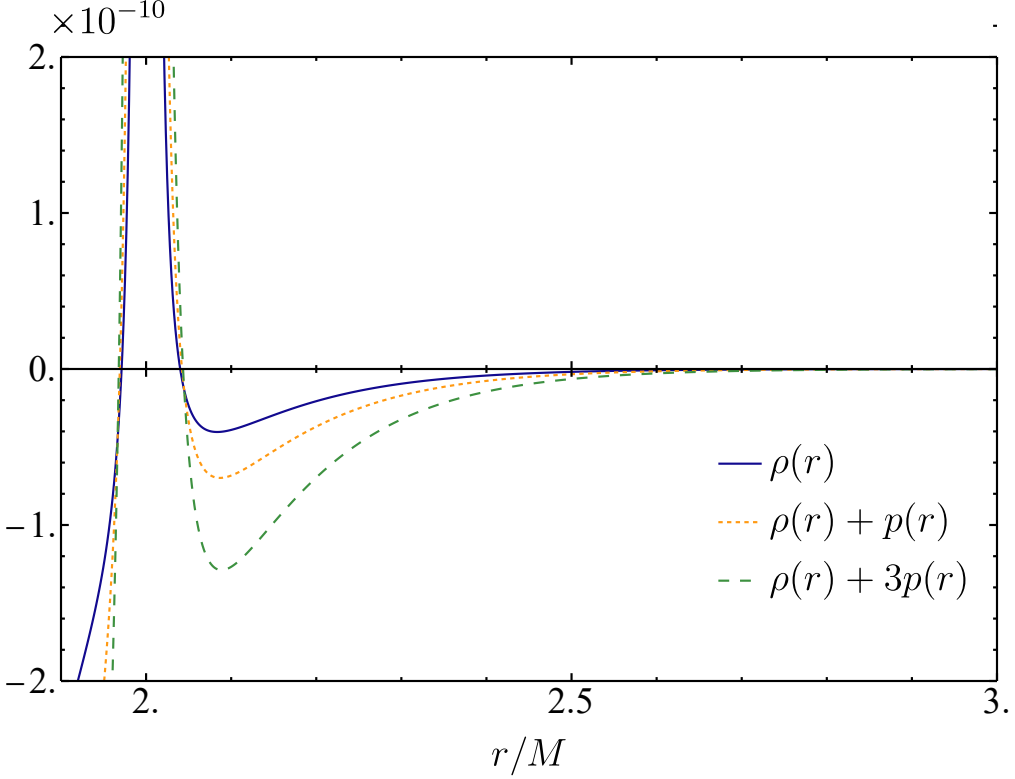


Figure 9: A visualization of the energy conditions in the weak-field regime computed using equations (69). The parameters are fixed at $\gamma = 1$, $\alpha = 1/2$, $\beta = 1/4$, $M = 10$, $S_2^- = 1/2$, and $S_0^- = 1/10$.

5. PROBING THE GEOMETRY BY SHADOW IMAGING

In the previous sections we have identified a number of solution classes and used them to construct a phase space. In reality, however, certain regions of the phase space will probably be not be physically possible. In General Relativity, for example, we only have one free parameter to which we ascribed the mass M . We know from observations that this parameter must be non-negative, but in the theory a negative mass is perfectly possible. In Quadratic Gravity we expect observations to do the same, isolate physically impossible regions from our phase space. To do observations within one of the solutions, we need to know the path particles take through the spacetime. This is done by the equations of motions from the geodesic equation

$$\frac{d^2x^\mu}{d\lambda^2} + \Gamma_{\alpha\beta}^\mu \frac{dx^\alpha}{d\lambda} \frac{dx^\beta}{d\lambda} = 0, \quad (74)$$

where λ is a scalar parameter. For massive particles we can choose $\lambda = \tau$, the proper time of the particle. This assures the normalization $1 = -g_{\mu\nu} \frac{dx^\mu}{d\tau} \frac{dx^\nu}{d\tau}$. Massless particles instead move along null trajectories

$$0 = -g_{\mu\nu} \frac{dx^\mu}{d\lambda} \frac{dx^\nu}{d\lambda}, \quad (75)$$

thus not fixing λ . Since we aim to replicate how a telescope (like the Event Horizon Telescope) images the singularity, we will only consider the dynamics of massless particles, i.e. light rays. Using the metric ansatz

(21) we get the geodesic equations

$$\begin{aligned} \frac{d^2t}{d\lambda^2} + \frac{h'(r)}{h(r)} \frac{dt}{d\lambda} \frac{dr}{d\lambda} &= 0 \\ \frac{d^2r}{d\lambda^2} + \frac{f(r)h'(r)}{2} \left(\frac{dt}{d\lambda} \right)^2 + \frac{f(r)}{2f'(r)} \left(\frac{dr}{d\lambda} \right)^2 - rf(r) \left[\left(\frac{d\theta}{d\lambda} \right)^2 + \sin^2 \theta \left(\frac{d\phi}{d\lambda} \right)^2 \right] &= 0 \\ \frac{d^2\theta}{d\lambda^2} + \frac{2}{r} \frac{d\theta}{d\lambda} \frac{dr}{d\lambda} - \sin(\theta) \cos(\theta) \left(\frac{d\phi}{d\lambda} \right)^2 &= 0 \\ \frac{d^2\phi}{d\lambda^2} + \frac{2}{r} \frac{d\phi}{d\lambda} \frac{dr}{d\lambda} + \frac{2\cos(\theta)}{\sin(\theta)} \frac{d\theta}{d\lambda} \frac{d\phi}{d\lambda} &= 0. \end{aligned} \quad (76)$$

Solving these analytically is again out of the question. Like before we can use numerical integration to trace the path of a light ray. This procedure will be discussed in the sequel, but first we will continue the theoretical analysis. Besides the geodesic equation, we can use the static nature and spherical symmetry of the system to constrain the motion of particles in the spacetime. This is done through Killing vectors K^μ for which

$$K_\mu \frac{dx^\mu}{d\lambda} = \text{constant}. \quad (77)$$

The Killing vector $K_E^\mu = (1, 0, 0, 0)$ relates to the static nature of the spacetime. The constant of motion related to this vector is the energy of the system E , hence the subscript in K_E^μ . Evaluating equation (77) yields an expression for the energy

$$E = h(r) \frac{dt}{d\lambda}, \quad (78)$$

where we have absorbed the negative sign into the definition of E .

For spherical symmetry, the accompanying constant of motion is the angular momentum \vec{L} . The direction of \vec{L} confines any particle's motion to a plane in three dimensional space. The spacetime can be freely rotated due to the symmetry such that this plane coincides with the equatorial plane $\theta = \frac{\pi}{2}$. Fixing θ reduces the constant of motion to just the magnitude of the angular momentum L , that belongs to the Killing vector $K_L^\mu = (0, 0, 0, 1)$. We can express the angular momentum as

$$L = r^2 \frac{d\phi}{d\lambda}.$$

We then substitute these conserved quantities into 75. Fixing $\theta = \frac{\pi}{2}$, this yields

$$-\frac{1}{h(r)} E^2 + \frac{1}{f(r)} \left(\frac{dr}{d\lambda} \right)^2 + \frac{L^2}{r^2} = 0.$$

This can be solved for $\frac{dr}{d\lambda}$,

$$\left(\frac{dr}{d\lambda} \right)^2 = L^2 \frac{f(r)}{h(r)} \left(\frac{1}{b^2} - V_{\text{eff}}(r) \right) \quad \text{where} \quad b = \frac{L}{E}, \quad V_{\text{eff}} = \frac{h(r)}{r^2}. \quad (79)$$

We have defined V_{eff} so help visualize this equation as a relation between the "energy budget" of the system. On the left-hand side is the kinetic energy and on the right hand side the total energy subtracted by some effective potential energy. We will from now on call b the impact parameter due to the role it plays in the ray tracing. Following the calculations done before in [38, 39], we can find the radii at which circular orbits are allowed by requiring $\frac{dr}{d\lambda} = 0$ and $\partial_r \frac{dr}{d\lambda} = 0$. The resulting system

$$r^2 - b^2 h(r) = 0, \quad (80)$$

$$\frac{2h(r)}{r^3} - \frac{h'(r)}{r^2} = 0 \quad (81)$$

$$(82)$$

can be quickly solved. The second equation

$$r_{\text{ph}} = \frac{2h(r_{\text{ph}})}{h'(r_{\text{ph}})}, \quad (83)$$

gives the photon radius, where photons can move in a circular orbit. The first equation then relates r_{ph} and the critical value for b

$$b_{\text{crit}} = \frac{r_{\text{ph}}}{\sqrt{h(r_{\text{ph}})}}, \quad (84)$$

for which a light ray will end up in this photon orbit. Consequently, the value of b_{crit} is the apparent radius seen by observation if done from sufficiently far away (which we assume will be the case). This radius will be called the shadow radius

$$r_{\text{sh}} = b_{\text{crit}} \quad (85)$$

For Schwarzschild black holes these values are well-known to be $r_{\text{ph}} = 3M$ and $r_{\text{sh}} = 3\sqrt{3}M$, which follow from equations (83) and (84) when substituting $h(r)$. The angular radius of the black hole's photon ring in the sky can be calculated with $\theta_{\text{ph}} = \frac{r_{\text{ph}}}{D}$, where D is the distance from the observer to the singularity. Observations of the M87 black hole the Event Horizon Telescope have measured $\theta_{\text{ph}} = 42 \pm 3 \mu\text{as}$, this justifies the assumption that the observer is far away from the center of the spacetime.

From the solutions to Quadratic Gravity we have analyzed, we have seen that they closely follow Schwarzschild until near $r = 2M$. The photon orbit, and consequently the shadow radius, can thus to good precision be evaluated in the weak-field regime. We can use the linear solutions for f and h in (40) in equation (83), keeping only linear terms results in

$$r_{\text{ph}} = 3M - 3S_2^- (m_2 M + 1) e^{-3m_2 M} - \frac{3}{2} S_0^- (m_0 M + 1) e^{-3m_0 M}, \quad (86)$$

and the conditions $3m_0 M \gg 1$ and $3m_2 M \gg 1$. The radius of the shadow is completely determine by the spacetime at radii greater than r_{ph} so the linearization holds for this calculation as well. Taking the result above and plugging it into equation (84) yields to linear order

$$r_{\text{sh}} = 3\sqrt{3}M - 3\sqrt{3}S_2^- e^{-3m_2 M} - 3\sqrt{3}S_0^- e^{-3m_0 M}, \quad (87)$$

We can immediately see that it is identical to the shadow radius for Schwarzschild plus two additional terms dependent on S_2^- and S_0^- respectively. We define a new parameter, ζ , to be the deviation of the shadows position compared to Schwarzschild

$$\zeta := \frac{r_{\text{sh}} - r_{\text{sh}}^{\text{SS}}}{r_{\text{sh}}^{\text{SS}}}. \quad (88)$$

We can compute this deviation for some realistic values to get a sense for the effects of Quadratic Gravity as a quantum mechanical theory, where we will take S_0^- for simplicity. Starting with the assumption $m_2 = m_{\text{pl}}$, the Planck mass, based on our expectation that the ghost masses will be the origin of quantum mechanical effects once the theory becomes quantized. Now, taking the mass of the black hole M87* as a rough estimate for a "normal" mass, $M = 2.2 \times 10^{50} m_{\text{pl}}$, we evaluate the deviation from Schwarzschild to be

$$\zeta = -e^{-6.6 \times 10^{50}} S_2^- . \quad (89)$$

While we cannot say much about the parameter S_2^- , it would be hard to believe that it will be of the size to have this result stray away from what is realistically just zero. We can thus conclude — what is already expected from a quantized theory of gravity — that quadratic gravity will not significantly modify the photon radius, other effect are much more prominent.

5.1 Intensity profiles

Instead we can look at a different observable that is affected by the quadratic contribution to the action. The matter surrounding a singularity will emit radiation, whose path can be traced towards an observed, creating an intensity profile. These profiles are related to the way the Event Horizon Telescope does its

observations and thus relevant in this context. We choose an elementary model introduced in [17] for its ease of use and capability of producing quality results at moderate numerical costs. We model an spherically symmetric, optically thin, and radially free-falling accretion model for the matter. Imposing spherically symmetry reflects the symmetry of the spacetime. Having the matter optically thin means we do not have the matter interact with any of the emitted radiation.

The matter will emit monochromatic radiation with frequency ν_* . Per unit volume the emissivity in the frame of reference of the emitting matter will be

$$j(\nu_e) \propto \frac{\delta(\nu_e - \nu_*)}{r^2}, \quad (90)$$

such that the total emission is constant across the radial shells surrounding the singularity. The intensity of the light will be measured by a stationary observer far away from the singularity $D \gg M$. The intensity on the screen of the observer will then depend on the coordinates on the screen, X and Y , and ν_{obs} , the observed frequency of the light ray,

$$I(\nu_{\text{obs}}, X, Y) = \int_{\gamma} g^3 j(\nu_e) dl_{\text{prop}}. \quad (91)$$

Here $g = \frac{\nu_{\text{obs}}}{\nu_e}$ is the redshift factor, γ is the path traveled by the light ray and dl_{prop} is an infinitesimal proper length along the path measured from the frame of the emitting mass. We can express the above quantities in the four-velocities of the emitting mass u_e^μ and the observer u_{obs}^μ and the four-momentum of the emitted light ray k^μ . The observer is stationary so $u_{\text{obs}}^\mu = (1, 0, 0, 0)$. The emitting matter is radially free-falling, setting $u_e^\theta = u_e^\phi = 0$, and has to satisfy $1 = -g_{\mu\nu} u_e^\mu u_e^\nu$, $h(r) u_e^t = 1$, and $u_e^r < 0$ resulting in

$$u_e^\mu = \left(\frac{1}{h(r)}, -\sqrt{\frac{1-h(r)}{h(r)}} f(r), 0, 0 \right). \quad (92)$$

The four-momentum of the photon can be derived from equation (79), yielding

$$k_\mu = \left(E, \pm \frac{E}{f(r)} \sqrt{\left(\frac{1}{h(r)} - \frac{b^2}{r^2} \right) f(r)}, 0, , L \right). \quad (93)$$

Depending on whether the photon moves radially inwards or outwards the k^r term has a $-$ or $+$ factor respectively. We can now express the redshift factor in terms of k^μ and the metric functions,

$$\begin{aligned} g_{\pm} &= \frac{\nu_{\text{obs}}}{\nu_e} = \frac{k_\mu u_{\text{obs}}^\mu}{k_\nu u_e^\nu} = \frac{E}{E/h(r) \mp \left(\frac{E}{f(r)} \sqrt{\left(\frac{1}{h(r)} - \frac{b^2}{r^2} \right) f(r)} \right) \sqrt{\frac{1-h(r)}{h(r)} f(r)}} \\ &= \left(\frac{1}{h(r)} \mp \frac{|k_r|}{k_t} \sqrt{\frac{1-h(r)}{h(r)} f(r)} \right)^{-1}. \end{aligned} \quad (94)$$

Like the photon's four-momentum, the sign in the equation for the redshift depends on if the photon is traveling radially outward (+) or inwards (-) respectively. Likewise, the proper distance can be expressed in terms of components of k_μ

$$dl_{\text{prop}} = k_\mu u_e^\mu d\lambda = \frac{k_\mu u_{\text{obs}}^\mu}{g} \frac{d\lambda}{dr} dr = \frac{k_t}{g|k_r|} dr. \quad (95)$$

We can now substitute these results as well as the emissivity (90) into equation (91) and integrate both sides over all observable frequencies to get

$$I_{\text{obs}}(X, Y) \propto \int_{\gamma} \frac{g^3 k_t}{r^2 |k_r|} dr. \quad (96)$$

Since we place the observer sufficiently far from the singularity we can express $X^2 + Y^2 = b^2$. Moreover, spherical symmetry allows us to express the intensity as a function of the impact parameter b only. We can

take a quick look in comparing how the two definitions for the impact parameter relate. On one hand the impact parameter is the ratio of angular momentum and the energy of the photon, $b = \frac{L}{E}$, while on the other hand it measures the position on the screen on the observer (whose center is of course aligned with the singularity) via $b^2 = X^2 + Y^2$. Since the spacetime is entirely static, the path of a photon from the point of emission to the observer is identical to the reverse process, where the observer emits the photon and the photon is "observed" by the accreting matter.

We have the critical impact parameter b_{crit} to be have the value for which an incoming photon enters the photon sphere. Its value is thus directly translated into a radius on the observer's screen, which we have called the shadow radius.

The ray tracing distinguishes the two regions of b , separates by b_{crit} . For $b < b_{\text{crit}}$ we either decrease the angular momentum of the light ray, lowering the potential energy barrier at the photon radius, or we increase the energy of the light ray so it is enough to go over the energy barrier in the effective potential as seen in figure 2. Either way, for $b < b_{\text{crit}}$ light rays will vanish in the case of a Schwarzschild black hole. On the observer's screen this region is simply the disk whose edge is the shadow radius as seen in figure 10a.

For $b > b_{\text{crit}}$ we either increase the angular momentum of the light ray, heightening the potential barrier at the photon radius, or the photon does not longer have enough energy to overcome the potential barrier. Either way, these photons end up in the accretion disk and are thus seen as a spot with a certain intensity on the observer's screen.

Computing the intensity profiles of the Quadratic Gravity solutions can now be done be tracing the path of a light ray backwards in time for every value of the impact parameter, and summing the intensity contributions along this path. We put the screen far away from the center of the spacetime, $D = 10^5 M$. The trajectory of the photon is completely determined by its four-momentum (93) and the value of the impact parameter b . There are two types of trajectories possible. If at any point along the trajectory $k^r = 0$, the photon is at a turning point after which k^r will flip sign and increase until it ends up in its accreting matter source. If the trajectory does not contain a turning point, the photon will continuously fall towards the singularity.

It is easy to figure out which value of b leads to which case. By solving equation (80) we either find value(s) of r that will be the turning point (finding multiple solutions is of course possible, but the only physically relevant solution appears at the largest radius), or there are no solutions and there is no turning point. If there is no turning point, we can terminate the photon trajectory at $r = 2M$ for solutions with a horizon, or $r \approx 0$ for horizonless- solutions. Since it is only until this point that a photon can actually be emitted by the accreting matter. The intensity then follows from doing the numerical integration of equation (96) from the observer to $r = 2M$, the motion will be continuously outward, so there is no sign change in k^μ or g . If there is a turning point, however, the trajectory of the photon will be comprised of an ingoing and outgoing segment. We can calculate the total contribution to the intensity by separately doing the numerical integration over these segments. We first calculate the radius of the turning point r_{turn} , then compute the outgoing part with the corresponding signs i.e. integrating from D to r_{turn} . Finally, we integrate the ingoing part, with the opposite signs from r_{turn} to ∞ . For practical reasons we cap this integral at the same value D since the emissivity of accreting matter outside this radius is negligible ($\sim 10^{-10}$).

The results for every solution class can be found in figure 10, where solutions with indistinguishable intensity profiles have been grouped together. In the top row we have plotted the relation between the intensity and the impact parameter. The bottom row used the spherical symmetry of the system to visualize how the observer would observe the singularity on their screen. These results require some further elaboration, and we will discuss them type by type.

We start off with the Schwarzschild solution in figure 10a. The critical impact parameter is exactly at $3\sqrt{3}M \approx 5.196$. Approaching this point from greater values of β sees the intensity smoothly increasing until it reaches a maximum at the critical impact parameter. Then the intensity suddenly drops to a low value that is due to foreground radiation. This drop results in the dark region in the image. We will already make the comparison with all other solution types now that the intensity plot for $b > b_{\text{crit}}$ are virtually indistinguishable. We expect this since for $r > 3M$ the corrections in the metric are exponentially. This again shows that the quadratic corrections to the action do not measurable influence the spacetime in the weak-field regime.

The Type I family of solutions is characterized by the scaling behavior $(-2, 2)_0$. We have introduced the three sub-types exactly because the quadratic scaling causes the effective potential at zero to be finite.

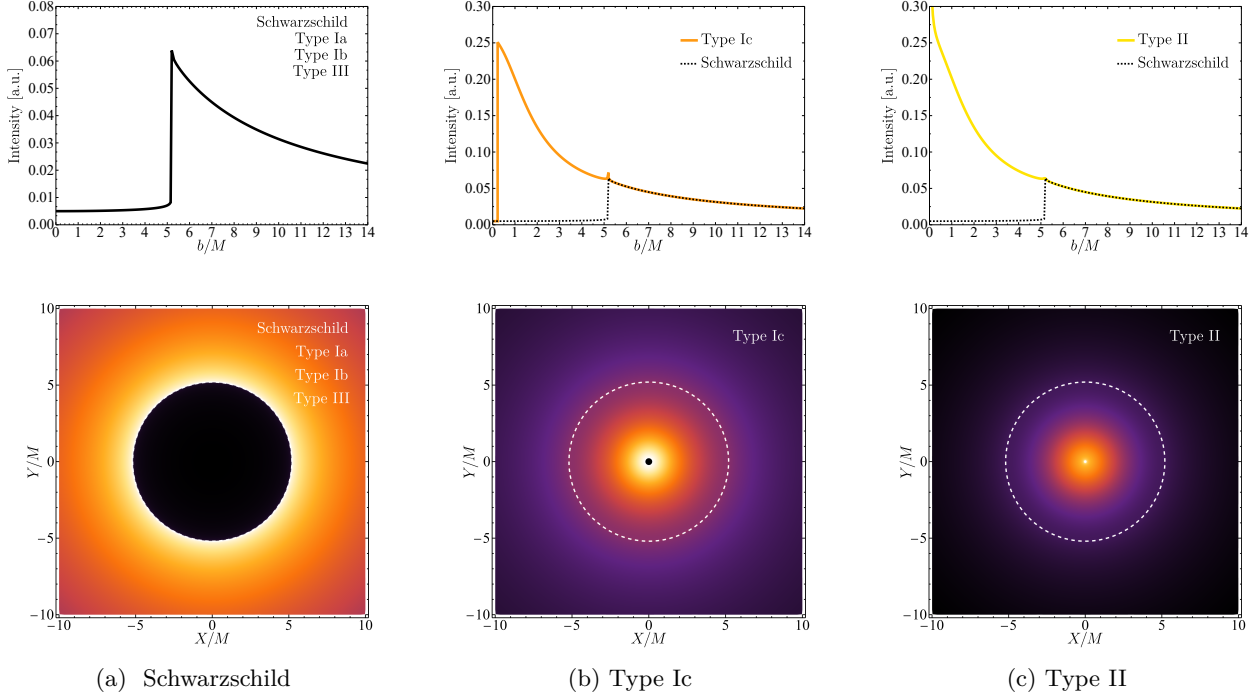


Figure 10: Distinguished intensity profiles obtained from the emission model (96) for spacetimes obtained from the initial conditions listed in Table 2. The left column shows the intensity for a Schwarzschild black hole with $M = 10$ (top row). This intensity profile is virtually indistinguishable from naked singularities of Type Ia, Type Ib, and Type III. The middle column gives the intensity for the Type Ic solution with initial conditions. The size of the shadow of a Schwarzschild black hole is added as a dashed line for reference. The presence of an inner turning point significantly enhances the intensity in the region $b_{\text{tp2}} \leq b \leq b_{\text{crit}}$. Intensity profiles for Type II solutions illustrated in the right column do not exhibit a shadow; their image resembles the one of a star with the peak intensity at small impact parameter b .

Type Ia encompasses the solutions whose effective potential monotonically decreases for $r < 2M$. For Type Ib the effective potential does not decrease monotonically — instead containing a well with a minimum — but the maximum value of $V_{\text{eff}}(r)$ stays at $r = 3M$. The result is that for both these solution classes the intensity plot does not differ from Schwarzschild. The critical impact parameter does not change compared to Schwarzschild, so we cannot probe the interior of the photon ring with this ray tracing method. This is remarkable as any observation of this kind that matches General Relativity through Schwarzschild, also matches Quadratic Gravity through these other solution classes. Thus an observation of this type cannot exclude one of the theories. The potential minimum of the Type Ib solution, however, would allow for elliptical photon orbits within the photon ring interior. We will briefly discuss the possibility of seeing effects of these orbits in the outlook.

The Type Ic class of solutions stands out within the Type I family as the effective potential for these solutions does extend above the potential barrier at $r = 3M$. Consequently, the critical impact parameter for these solutions can be smaller than that of Schwarzschild, leading to a decrease in shadow size. The resulting intensity profile for a solution within the Type Ic class can be found in figure 10b. We can see in this figure that the intensity within the white dashed circle representing the Schwarzschild shadow is much greater than the intensity outside it. The intensity picked up by the light rays that do cross the photon ring and reach the turning point within the photon radius thus is of higher magnitudes than what we get from Schwarzschild black holes.

The new critical impact parameter differs on a solution by solution. For some solutions, like the one in figure 10b, the difference is big enough that these can easily be ruled out from observations. There are, however, solutions where the black hole shadow will only shrink a minuscule amount compared to

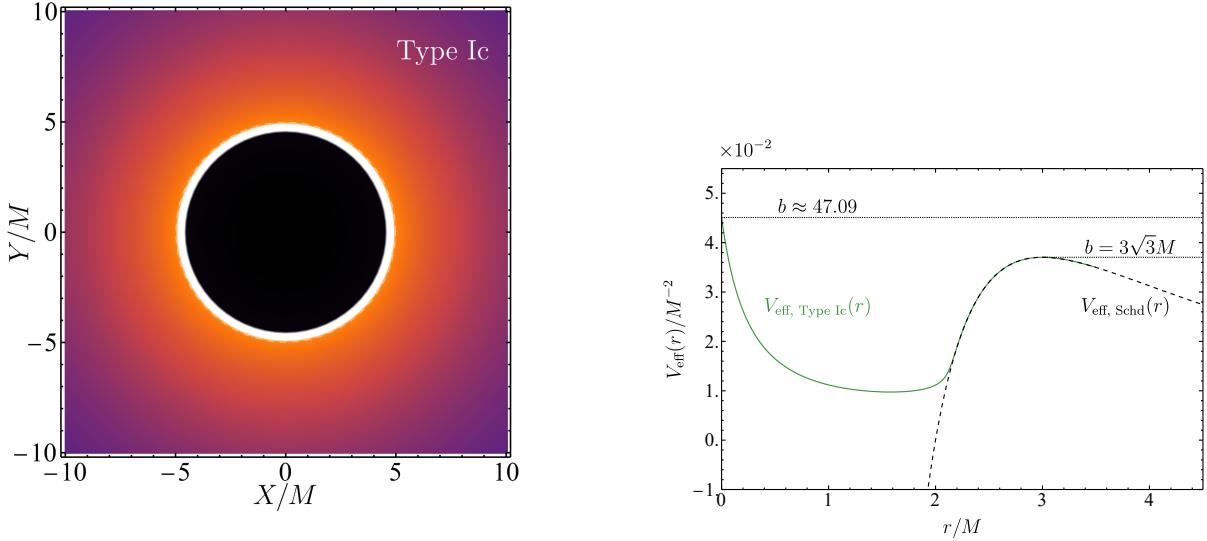


Figure 11: A Type Ic solution where $S_2^- = 1/2$, $S_0^- = -1/100$, and $\beta = 1/10$. On the left, the intensity profile for this solution based on the emission model in equation (96) is visualized. Superimposed on the image is a white dashed circle representing the shadow radius for a Schwarzschild black hole. On the right, the potential energy of the solution is plotted in green and the Schwarzschild potential is plotted in dashed black.

Schwarzschild. In figure 11 we have again a Type Ic solution, whose shadow does not differ a great amount from that of Schwarzschild. On the right side of the figure we have graphed the effective potential of the solution. Here we see that the new critical impact parameter decreases by less than 10% smaller compared to Schwarzschild. The result is that the presence of a shadow with a plausible radius based on General Relativity is not enough to guarantee that it actually is a black hole. It could very well be a Type Ic solution where the slight decrease of the shadow's radius is smaller than the observational resolution.

Instead of the radius of the shadow, the intensity surrounding the shadow is now the distinguishing factor between Schwarzschild and Type Ic. Light rays with an impact parameter between b_{crit} and $b_{\text{crit}}^{\text{SS}}$ have their turning point very close to the singularity. Consequently, their trajectory is longer and passes through a region where the emission from the accreting matter is high. The result is a significant increase of intensity in Type Ic solutions that cannot be explained by Schwarzschild. This feature does in fact mean that Type Ic solutions can be most likely ruled out by observations.

We proceed with discussing the Type II solution class that is defined by having the scaling behavior $(-1, -1)_0$. Near $r = 0$ we have $V_{\text{eff}}(r) \sim \frac{1}{r^2} = \frac{1}{r^3}$, i.e. the effective potential diverges. The singularity in this case is shielded by an infinite repulsive potential barrier and there will thus be no impact parameter for which there is no turning point. The result from the numerical integration, seen in figure 10c, indeed confirms that there is no shadow at all. Instead the central point is where the intensity is maximal. The intensity profile looks like that of a star rather than a black hole. These solutions might be similar to ultra compact objects like neutron stars [40, 41].

Finally, the Type III solution class is fundamentally different from the other classes as the numerical integration terminates at a termination point $r_{\text{term}} > 2M$. We have identified these solutions to be wormholes, where the radius r_{term} can also be interpreted as the throat of the wormhole. We can then stitch a different spacetime to the other side of the wormhole to extend our solution and simply state that any trajectory venturing within the wormhole throat will not be able to emerge and likewise no photons can appear from the wormhole from the other side. On this basis the wormhole throat is identical to an event horizon of a Schwarzschild black hole. Since the Type III solutions all terminate between $2M < r_{\text{term}} < 3M$ the photon ring is still present and will shield the spacetime within from being reached. Thus, solutions of Type III are

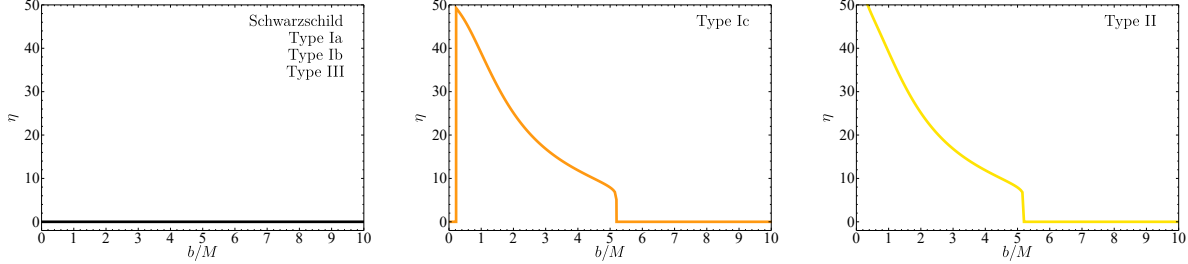


Figure 12: Relative difference in intensity, eq. (97) evaluated for geometries of Type Ia, Type Ib, and Type III (left), Type Ic (middle) and Type II (right) with mass $M = 10$. The latter two cases show distinguished and strong deviations from the Schwarzschild case, allowing to distinguish between the geometries based on shadow images.

indistinguishable from Schwarzschild as well.

We can summarize these results by introducing a new parameter η that measures the relative difference in the intensity compared to Schwarzschild,

$$\eta(I) \equiv \frac{I - I_{\text{Schwarzschild}}}{I_{\text{Schwarzschild}}} . \quad (97)$$

The value of η as a function of the impact parameter for the three possible intensity profiles can be seen in figure 12. We see that Type Ia, Type Ib and Type III solutions are indistinguishable from Schwarzschild. Type Ic and Type II solutions differ as soon as $b < 3\sqrt{3}M$, almost instantly gaining roughly a magnitude more intensity than Schwarzschild. This is due to an instantaneous jump in r_{turn} that suddenly allows for longer trajectories in more extreme regions of gravity. Finally, Type Ic and Type II differ in that the former has a shadow whereas the latter keeps its brightness until the center of the image.

One final important remark is that in observations it is the size of the shadow that is used to crosscheck the mass of the system with other observation channels. For Type II solutions, however there no longer is shadow to measure. Similarly, for Type Ic solutions there is a shadow, but it no longer relates to the mass as it does for Schwarzschild black holes. However, we notice in the intensity profiles of these solutions (figure 10b and 10c) that at $b = 3\sqrt{3}M$ there is a slight but sharp bump in the intensity. A measurement of this bump can be used to ascribe a mass scale to the system.

6. SUMMARY

In this work we have developed a framework for numerically constructing spacetime solutions for the theory of Quadratic Gravity. Using this framework we found solutions with distinct characteristics, which we used to introduce a number of solution classes. These numerical solution classes were then compared to analytical solution classes that were the result of a Frobenius analysis we performed. We then started the first explicit attempt at probing parts of the phase space and classifying the solutions according to our classification. We also performed an analysis of the region the solutions occupied in the phase space. This included treating the quadratic terms in Quadratic Gravity as an effective stress-energy tensor in General Relativity, resulting in a greater insight into the behavior of the identified numerical solutions. Finally, we put constraints on which solution classes are physically viable by constructing intensity profiles from an emission model of accreting matter. This profiling allowed us to eliminate two solution classes from appearing in nature, putting boundaries on the constructed phase space. To achieve this results, we employed the following strategy.

First, we assumed the spacetime to be static, spherically symmetric and asymptotically flat. We also restricted the analysis to solutions in vacuum ($T_{\mu\nu} = 0$) and with a vanishing cosmological constant ($\Lambda = 0$). On this basis we derived the equations of motion, which could be reduced to two coupled third order differential equations. An analysis on these equations of motions yielded that a solution has at most six degrees of freedom.

The approach to solving the equations of motion was to use a numerical algorithm, which only needed valid initial conditions. Getting the initial conditions was done by linearizing the equations of motion, a procedure that holds for large radius. The linearized equations of motion could be readily solved, yielding the Schwarzschild solution with four additional Yukawa modes. After asserting asymptotic flatness and normalizing the time coordinate, there remain three free parameters in the solution: the asymptotic mass of the system M , as well as two new parameters S_2^- and S_0^- . In addition to these parameters, the theory itself has three coupling constants γ , α , and β , which enter the linearized solutions through the spin-two ghost mass and spin-zero scalar mass. Finally, due to the numerical nature of the solving algorithm a point r_i where the initial conditions are imposed had to be chosen.

Using the linearized solutions as initial conditions, we proceeded to integrate the full equations of motion for roughly 6500 sets of parameters. Here, S_2^- , S_0^- , and β where taken variable while the remaining parameters where fixed across all point. All these solutions followed the Schwarzschild solution in the region $r > 2M$, but at a certain point rapidly deviated. We were able to identify six distinct solution classes based on their scaling behavior near the termination point of the numerical integration. These scaling behaviors matched the analytical results from a Frobenius analysis[5, 8].

The first solution recovered was the Schwarzschild solution, which solves both General Relativity and Quadratic Gravity. Secondly, two types naked singularities, differing by their scaling behavior, were identified and classified as Type I and Type II. The Type I solution, characterized by the g_{tt} component of the metric having quadratic scaling near the singularity, was further split into three subtypes, according to the effective potential of these solutions. Finally, solutions with a termination point $r_{\text{term}} > 2M$ where identified to be wormhole solutions and classified as Type III. This work features a three-dimensional slice of the phase space where this classification was used to differentiate the points in the phase space.

This result signifies that the Schwarzschild solution is the only solution in Quadratic Gravity ($\alpha \neq 0$, $\beta \neq 0$) with an event horizon for asymptotic masses greater than the maximum mass at which Stelle black holes appear [7]. This is in agreement with other findings [8] and suggests a uniqueness theorem similar to Birkhoff's theorem in General Relativity. *The only solutions to Quadratic Gravity compatible with the cosmic censorship hypothesis that is static, spherically symmetric and asymptotically safe are the Schwarzschild solution and Stelle black hole solution.*

We provided a detailed explanation to the artifacts resulting from the use of numerical methods. In showing the deviation of the numerical solutions from integer scaling we discussed the drawbacks of numerical integration and we argued for why the results should generally be unaffected.

We then performed an extensive analysis of the quadratic terms when they are treated as an effective stress-energy tensor in General Relativity. In some parts of the phase space it followed that Type III solutions are the result of an effective exotic matter configuration and as a result fail the energy conditions. In the

limit of large β , however, this correlation no longer held true, hinting that initial conditions do not strictly hold information on the resulting solution type.

In a further analysis to the individual components of the stress-energy tensor in the weak-field, we compared the effective stress-energy tensor with that of a perfect fluid. Here we found a relation between the parameters S_2^- , S_0^- and the energy and pressure density of a perfect fluid. We believe that this can provide insights into what these additional parameters in Quadratic Gravity can physically mean.

We followed the analysis of the phase space by an attempt to extract information from the newly found solutions that could be observed by the Event Horizon Telescope. We first showed that the radius of the photon orbit is undisturbed by the presence of the quadratic terms. This is evident from our solutions only diverging from the Schwarzschild solution at radii close to the would-be event horizon at $r = 2M$.

In order to probe these deviations in the interior of the photon ring, we equipped the solutions with the emission model suggested in [17]. Solutions of Type Ic and Type II are characterized by having a critical impact parameter b smaller than a Schwarzschild black hole in General Relativity, $b_{\text{crit}}^{\text{SS}} = 3\sqrt{3}M$. In the emission model this results in a sharp increase in intensity for values of b where one would in General Relativity expect only a feint amount. Type Ic differs from Type II in that the former does have a shadow, whereas the latter does not and the intensity peaks at $b = 0$. Solutions in both these categories can be ruled out by observations, putting restrictions on the parameters that make up the phase space.

Solutions of Type Ia, Type Ib and Type III all have the curvature singularity shielded, as all photons with $b < b_{\text{crit}}$ plunge into the singularity. This feature makes the geometries indistinguishable from a Schwarzschild black hole. On this basis alone, an observation cannot distinguish a black hole from a naked singularity or wormhole throat. Leading us to the main conclusion that — due to Quadratic Gravity being a possible extension to General Relativity — it is impossible in non-rotating spacetimes for the Event Horizon Telescope to conclude if it is actually observing an event horizon.

7. OUTLOOK

Quadratic Gravity is a useful candidate for a quantum theory of gravity. With this thesis we have confronted the theory with observational results. The steps taken in this thesis also pave the road for further research in this direction. We will now briefly discuss some interesting steps that can be taken in the future.

7.1 Further investigation of the phase space

In this research we have initiated the systematic search for solutions in the phase space. Having probed it as roughly 6500 point across three dimensions, there is a lot left to discover. Our analysis has found solutions across all relevant analytical classes from the Frobenius analysis (table 1), an extensive scan will hopefully find more structure in the way the solutions occupy the phase space.

Increasing the scale of the system

We probed the phase space along the parameters β , S_0^- , and S_2^- , which go a long way of probing a system for different initial conditions, but the scale of the system stays mostly constant. There are three ratios that can be considered important in understanding the scale of the system. We were able to vary the ratio $\frac{m_0}{m_2} \propto \frac{\alpha}{\beta}$ by changing β , with this variation we change which of the quadratic terms dominates the action. The other two ratios are $\frac{m_0}{M}$ and $\frac{m_2}{M}$, indicating the scale of the quadratic contributions compared to the asymptotic mass of the geometry. In our analysis of the phase space, this ratio was around $\frac{1}{10}$ for both m_2 and m_0 . Given that both the spin-two and spin-zero mode will be interpreted as quantum mechanical contributions, we can assume their size will be many orders of magnitude smaller than M . There will be little difference between the ratio $\frac{m_0}{M}$ and $\frac{m_2}{M}$, leaving two meaningful ratios to determine the mass hierarchy of the system. Probing the phase space for increasing values of M will be the first step in applying Quadratic Gravity on real astronomical scales. The study by Silveravalle [14] has started this by scanning a part of the phase space where the mass is taken as a variable.

Improving the numerical integration

In generating the solutions we have used the *stiffness switching* method of the numerical integrator in the proprietary software Mathematica. This integrator suffices in the exploratory scan of the phase space we have performed. Within this software there are a great amount of options available to refine the integration, something that was not done in our research.

A deeper investigation into the different numerical algorithms available for integration can help find one that is most suited to the dynamics of the system. When going to this level of refinement it might become necessary to write the source code for the algorithm, instead of using proprietary software that cannot be fine-tuned to the same level.

Optimizing the integration process will allow for more precise and accurate results. This will also allow the solutions to be generated starting from larger values of r_i , leading to less error prone representation of the phase space.

7.2 Imaging Type Ib solutions

In section 5 we have used an elementary emission model to numerically compute the intensity profile of all solution types. Here we found three distinct cases, Type Ic and Type II differed distinctly from a Schwarzschild black hole, while Type Ia, Ib and III were indistinguishable. In the model used could only probe to the radius where the impact parameter first intersected the effective potential. For Type Ia and Type Ib solutions this caused the potential peak at the photon radius to shield the potential within it from being examined.

The Type Ia solutions are defined as having a monotonically decreasing potential below $r \leq r_{\text{ph}}$. Any particle that exists within the photon radius will irreversibly go to the center of the spacetime, where it merges

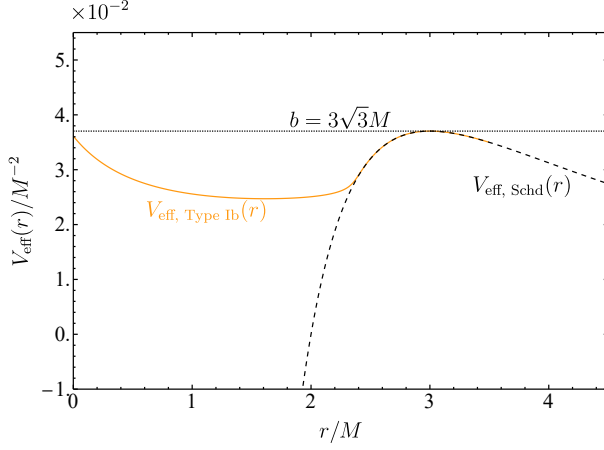


Figure 13: A Type Ib solution (in yellow) where the potential well at $r < r_{\text{ph}} = 3M$ lies close to the peak of the potential at the unstable photon orbit. The potential for the Schwarzschild solution is included in dashed black. The solution was generated using initial conditions $\alpha = 1/2$, $\beta = 1/24$, $S_2^- = 1/200$, $S_0^- = -1/5$, $M = 10$, and $r_i = 35$.

with the singularity. Therefore a more complex emission model will more likely not alter the intensity profile, keeping a Type Ia naked singularity indistinguishable from a Schwarzschild black hole.

In contrast, Type Ib solutions have a stable minimum within the unstable photon orbit at $r = 3M$. There is thus a second photon orbit, which is stable. The stable nature not only allows for circular orbits, but also elliptical ones. Like how the planets in the solar system orbit the sun, the singularity can have massless particles orbiting around it in many different orbits. The emission model we does not take such a phenomenon into account and would therefor need to be enhanced.

In such an enhanced emission model, the matter in the accretion disk will not be as simple as the radially freefalling matter we covered in our analysis. The presence of the stable minimum could result in the dynamics of the accretion disk become more complex. This would warrant the use of magnetic hydrodynamic simulations of the spacetime to find the density distribution of the luminous matter. This more complex distribution could then be used by a more advanced ray tracing algorithm to simulate intensity profiles.

A possible advanced ray tracing algorithm is RAPTOR [42, 43]. The use of RAPTOR will be first step at simulation these images at higher resolution with more elaborate details that our elementary approach lacks. This advanced algorithm can work with far more realistic accretion disk models, like the one discussed above, to create a detailed image of Type Ib solutions and how they can possibly differ from a Schwarzschild black hole.

7.3 Rotating solutions

The research covered in this thesis examines the phase space of solution in Quadratic Gravity. Furthermore we have constructed intensity profiles for these solutions that can be used in comparison with observations. Here, however, we stumble on a shortcoming of this research that will also serve as an outlook for future followup research; in reality most black hole candidates rotate. This breaks the spherical symmetry assumed in this work meaning the solution types we have introduced theoretically exist, but may not be the typical black holes observed in nature. Still these results do provide some merit in the approach to solving Quadratic Gravity for rotating solutions. Firstly, we have provided an extensive framework for probing the phase space which can — with undoubtedly some modifications — be used as a guideline for doing the same with rotating solutions. Secondly, any future rotating solution will depend in some way on the angular momentum of the system J . Taking the limit $J \rightarrow 0$ removes the rotation from the system, thus returning us to the spherical symmetry discussed here. Any rotating solution in this limit will have to reduce to a solution present in this

work.

We can make a start in finding rotating solutions and we will highlight some challenges that pop up after introducing rotation. Looking at General Relativity, rotating black hole spacetimes are described by the Kerr metric,

$$ds^2 = - \left(1 - \frac{r_s r}{\Sigma} \right) dt^2 + \frac{\Sigma}{\Delta} dr^2 + \Sigma d\theta^2 + \left(r^2 + a^2 + \frac{r_s r a^2}{\Sigma} \sin^2 \theta \right) \sin^2 \theta d\phi^2 - \frac{2r_s r a \sin^2 \theta}{\Sigma} dt d\phi. \quad (98)$$

Here (with $c = G = 1$ for consistency) $r_s = 2M$, the Schwarzschild radius, $a = \frac{J}{M}$, $\Sigma = r^2 + a^2 \cos^2 \theta$, and $\Delta = r^2 - r_s r + a^2$. We clearly see that spherical symmetry is broken and only axial symmetry remains, i.e., no metric component depends on ϕ . Furthermore, we no longer have a diagonal metric, further increasing the complexity of this solution compared to Schwarzschild. As before we would like to know if this Kerr metric even is solution to Quadratic Gravity. Since it solves pure General relativity we know that $R = 0$ and $R_{\mu\nu} = 0$. Kerr thus automatically solves the equations of motions stemming from R^2 in the action (31). The only term in (32) we explicitly have to compute is $\nabla^\rho \nabla^\sigma C_{\mu\rho\nu\sigma}$, which is zero for the Kerr metric.

With the Kerr metric a solution we can use its form as a template for constructing a generalized static, axially symmetric metric

$$ds^2 = -A(r, \theta)dt^2 + B(r, \theta)dr^2 + Y(r, \theta)d\theta^2 + Z(r, \theta)d\phi^2 - 2X(r, \theta)dt d\phi. \quad (99)$$

Plugging in this metric ansatz into the full equations of motion (32) yields equations many orders of magnitude larger than the spherically symmetric ones. See appendix B for the procedure used in this computation. From these equations it is immediately evident that solutions will not be easy to find. Using numerical integration will be a lot more time consuming due to the metric functions now having two variables. With enough effort numerical integration will be possible, but more effort will have to go in the optimization of the procedure.

Also important for numerical integration is getting good initial conditions to start the integration with. Here we also run into a problem that wasn't present in the spherically symmetric case. Linearizing the equations of motion should again prove a good approach to generating initial conditions. Schwarzschild is unique in the sense that it is already a linearized solution, hence it solved both the equations of motion (34) and the linearized equations of motion (38). Kerr, however, does not solve the linearized equations of motion for the metric (99). It thus is no longer as easy as having a solution to General Relativity and attaching some exponentially decaying modes to generate initial conditions.

There are of course still ways to go about finding linear solutions. Since Kerr solves the full equations of motion, a linearized Kerr metric has to solve the linearized equations of motion. We can define the linear regime as before and drop all terms of order r^{-2} or higher. For the g_{tt} and g_{rr} components we find

$$g_{tt} = - \left(1 - \frac{r_s}{r} \frac{1}{1 + \frac{a^2}{r^2} \cos^2 \theta} \right) = - \left(1 - \frac{r_s}{r} \right) + \mathcal{O}(r^{-2}) \quad (100)$$

$$g_{rr} = \frac{1 + \frac{a^2}{r^2} \cos^2 \theta}{1 - \frac{r_s}{r} + \frac{a^2}{r^2}} = 1 + \frac{r_s}{r} + \mathcal{O}(r^{-2}). \quad (101)$$

Meaning that $A_{\text{lin}}(r) = 1 - \frac{r_s}{r}$ and $B_{\text{lin}}(r) = 1 + \frac{r_s}{r}$ are just Schwarzschild and do no longer dependent on θ . For the $g_{\theta\theta}$ and $g_{\phi\phi}$ components we will also use that in the linearized regime $r \gg a$ and $r \gg r_s$, so we will also drop terms that are overall quadratic the length scales a and r_s ,

$$g_{\theta\theta} = r^2 + a^2 \cos^2 \theta = r^2 + \mathcal{O}(a^2) \quad (102)$$

$$g_{\phi\phi} = \left(r^2 + a^2 + \frac{r_s a^2}{r} \frac{1}{1 + \frac{a^2}{r^2} \cos^2 \theta} \sin^2 \theta \right) \sin^2 \theta = r^2 \sin^2 \theta + \mathcal{O}(a^2). \quad (103)$$

The angular metric components completely resolve to Schwarzschild as well, i.e. $Z_{\text{lin}}(r, \theta) = Y_{\text{lin}}(r, \theta) = 0$. It is only when we linearize the off diagonal term $g_{t\phi}$ that we see a difference to Schwarzschild

$$g_{t\phi} = - \frac{2r_s r a \sin^2 \theta}{\Sigma} = - \frac{2r_s a \sin^2 \theta}{r} \frac{1}{1 + \frac{a^2}{r^2} \cos^2 \theta} = - \frac{2r_s a \sin^2 \theta}{r} + \mathcal{O}(r^{-2}). \quad (104)$$

Thus $X_{\text{lin}}(r, \theta) = \frac{r_s a \sin^2 \theta}{r}$ is the only additional term in the linearized Kerr metric that differentiates it from (linearized) Schwarzschild. Plugging in these linearized solutions indeed solve the linearized equations of motion. More importantly with the linearized Kerr solution we can make some general assumptions on the linear functions. First, we will limit A_{lin} and B_{lin} to only be dependent on r . Second, we set $Z_{\text{lin}}(r, \theta) = Y_{\text{lin}}(r, \theta) = 0$. We only keep X_{lin} unchanged.

Plugging these general assumptions into the linear equations of motion, the diagonal components return to exactly those in the spherically symmetric case, i.e. X_{lin} does not make an appearance. Similarly, there is an off diagonal term in the equations of motion $H_{r\theta}^{\text{lin}}$, that automatically vanishes with this assumption. Finally, the off-diagonal part $H_{t\phi}^{\text{lin}}$ is the only equation in which X_{lin} appears, and it is the only function to appear.

This means that the linear solutions are largely unchanged from the spherically symmetric solutions. The diagonal terms and thus the traces solve the same way. Consequently, the same Yukawa modes are still a solution as well. The only difference then comes from the off diagonal term $X_{\text{lin}}(r, \theta)$. Linear Kerr gives us a baseline to use for this function, but it would be interesting to introduce a slight perturbation like we did for A_{lin} and B_{lin} . One possible perturbation can be found by stating that it will be independent on θ — like the other perturbations. The linear equation of motion severely reduces with this ansatz to

$$\frac{1}{2} X''_{\text{lin}}(r) - \alpha X^{(4)}_{\text{lin}}(r) = 0. \quad (105)$$

This equation can be completely solved, where the only asymptotically flat solution is

$$X_{\text{lin,pert}}(r) = X_2^- e^{-m_2 r}. \quad (106)$$

This introduces a new parameter that is completely independent from S_2^- and S_0^- , but the result is still dependent on the spin-two mass. With this result we have a first way to generate initial conditions in the weak-gravity regime for the rotating solutions. There is only one extra parameter introduced and only one function to incorporate a θ -dependence. This thus might be a good starting point for finding alternative solutions for spacetimes with a rotating central mass.

Though one other obstacle is the lack of a theoretical Frobenius analysis of the equations of motion for the general metric. This analysis will also be difficult due to the dependence on θ . While not necessary for the numerical integration, it means a comparison to analytical methods will be more complicated.

The Newman Janis algorithm

There are undoubtedly more solutions to be found. A method that might also provide insights is the use of the Newman-Janis algorithm [44]. This algorithm constitutes of a coordinate transformation as well as complexification of the coordinates. In this way one can derive the Kerr solution from the Schwarzschild solution in General Relativity[45].

As both the Schwarzschild and Kerr solution also solve the equation of motion in Quadratic Gravity, its applicability might be extended to this theory. It might be possible to apply the algorithm to the additional Yukawa terms we introduce in the weak-field regime, to generate a set of perturbations we can subsequently add to the linearized Kerr solution. This could be another way to generate initial conditions for the equations of motions of a static, axially symmetric space time.

However, it is not completely understood how the algorithm works and to what extend it works. It might only give part of the complete solution, or it could not work at all and the cases in which it does work are coincidental. There is definitely a chance that the algorithm will not be the right approach, but it is worth trying. It can still give insights in solutions that otherwise might not be discovered.

7.4 Extending wormhole solutions

Unique to the Type III solutions, the termination point of the numerical integration is not a true singularity, merely the coordinate system we use becomes singular. We have identified these solution as wormholes, where the termination point of the integration is the radius of the throat of the wormhole. Consequently, the Type III solutions we have generated are incomplete, as spacetime continues on the other side of the wormhole.

7 OUTLOOK

Following the setup used in a recent study [13], it should be possible to extend the wormhole solutions to fully cover all of spacetime. This procedure introduces a coordinate transformation for the radius

$$r = r_{\text{throat}} + \frac{1}{4} \rho^2. \quad (107)$$

The new variable ρ can take both positive and negative values, where the positive values indicate one side of the wormhole and negative values the other side. We have considered the Type III solutions to be part of the analytic solution class $(1,0)_{r_0}$, the result of our Frobenius analysis. In the Frobenius ansatz the metric components are expressed as a series of integer powers of r . The above coordinate transformation will consequently only contain even integer powers of ρ , meaning the spacetime is symmetric in the wormhole throat. Such a wormhole is thus called a symmetric wormhole.

However, in the Frobenius analysis we performed, we only included whole integer powers of $r - r_0$. It is possible to also include half-integer powers, which introduces additional solution classes. The analysis in [8] yields an additional solution class that is of interest here, $(1,0)_{\sqrt{r-r_0}}$. The half-integer analysis extends the $(1,0)$ solution class, doubling the number of free parameters from three to six. The half integer terms in the ansatz will pick up on the sign of ρ , thus breaking the symmetry. Solutions identified as Type III are part of this bigger overarching class and can thus be either symmetric or non-symmetric wormholes.

The study by Bonanno et al. [13] investigates these non-symmetric wormholes in the Einstein-Weyl theory (i.e. $\beta = 0$). Applying the procedure to the solutions presented in this work will allow the construction of non-symmetric wormholes in the full theory of Quadratic Gravity.

8. ACKNOWLEDGMENTS

I sincerely thank Frank Saueressig for his superb supervision and for taking me along in this new and exciting research. It was a pleasure to be introduced to Jesse Daas who had already spent some time on the foundations for this research and quickly got me up to speed. When a few months later Michael Florian Wondrak joined in on the research, bringing along his expertise of the Event Horizon Telescope, the team was complete. It was a joy to meet every week, even though it was especially early for me. I am thankful for the trust that was put in me and for the opportunity to work from home, allowing me to venture for the better part of the year to Chile. I am grateful to Máximo Bañados for inviting me to his department and letting me share our findings. Finally, I cannot go without thanking my girlfriend Constanza for supporting me throughout this year and motivating me by showing a great amount of interest in my work. Thank you all for this wonderful experience.

REFERENCES

1. T. L. S. Collaboration, the Virgo Collaboration, *Physical Review Letters* **116**, 061102 (Feb. 11, 2016).
2. K. Akiyama *et al.*, *Astrophys. J. Lett.* **875**, L1 (2019).
3. M. Kramer *et al.*, *Physical Review X* **11**, 041050 (Dec. 13, 2021).
4. C. M. Will, *Living Reviews in Relativity* **17**, 4 (Dec. 2014).
5. K. S. Stelle, *General Relativity and Gravitation* **9**, 353–371 (Apr. 1, 1978).
6. A. Salvio, *Frontiers in Physics* **6** (Aug. 2018).
7. H. Lu, A. Perkins, C. N. Pope, K. S. Stelle, *Physical Review Letters* **114**, 171601 (Apr. 28, 2015).
8. H. Lü, A. Perkins, C. N. Pope, K. S. Stelle, *Physical Review D* **92**, 124019 (Dec. 9, 2015).
9. H. Lü, A. Perkins, C. N. Pope, K. S. Stelle, *Int. J. Mod. Phys. A* **30**, 1545016 (2015).
10. B. Holdom, *Physical Review D* **66**, 084010 (Oct. 16, 2002).
11. J. Podolsky, R. Svarc, V. Pravda, A. Pravdova, *Physical Review D* **101**, 024027 (Jan. 8, 2020).
12. A. Bonanno, S. Silveravalle, *Journal of Cosmology and Astroparticle Physics* **2021**, 050 (Aug. 1, 2021).
13. A. Bonanno, S. Silveravalle, A. Zuccotti, *Physical Review D* **105**, 124059 (June 24, 2022).
14. S. Silveravalle (Feb. 2, 2022).
15. F. Saueressig, M. Galis, J. Daas, A. Khosravi, *Int. J. Mod. Phys. D* **30**, 2142015 (2021).
16. C. Bambi, *The Astrophysical Journal* **761**, 174 (Dec. 20, 2012).
17. C. Bambi, *Physical Review D* **87**, 107501 (May 3, 2013).
18. A. Held, R. Gold, A. Eichhorn, *Journal of Cosmology and Astroparticle Physics* **2019**, 029–029 (June 2019).
19. K. Akiyama *et al.*, *Astrophys. J. Lett.* **930**, L12 (2022).
20. J. Daas, K. Kuypers, F. Saueressig, M. F. Wondrak, H. Falcke, *arXiv:2204.08480* (Apr. 18, 2022).
21. A. Einstein, in *The Meaning of Relativity* (Springer, 1922), pp. 54–75.
22. H. Falcke, F. Melia, E. Agol, *The Astrophysical Journal* **528**, L13–L16 (Jan. 1, 2000).
23. S. Carroll, *Spacetime and Geometry: An Introduction to General Relativity* (Cambridge University Press, 2019).
24. K. Schwarzschild, *Sitzungsber. Preuss. Akad. Wiss. Berlin (Math. Phys.)* **1916**, 189–196 (1916).
25. C. H. McGruder III, B. W. VanDerMeer (Jan. 21, 2018).
26. S. W. Hawking, G. F. R. Ellis, *The Large Scale Structure of Space-Time* (Cambridge University Press, 1973).
27. C. Kiefer, *Quantum Gravity: Third Edition* (OUP Oxford, 2012).
28. R. Loll, *Classical and Quantum Gravity* **37**, 013002 (Dec. 2019).
29. M. Reuter, F. Saueressig, *Quantum Gravity and the Functional Renormalization Group: The Road towards Asymptotic Safety* (Cambridge University Press, 2019).
30. G. 't Hooft, M. J. G. Veltman, *Ann. Inst. H. Poincaré Phys. Theor. A* **20**, 69–94 (1974).
31. M. H. Goroff, A. Sagnotti, *Nucl. Phys. B* **266**, 709–736 (1986).
32. S. Weinberg, presented at the 17th International Conference on High-Energy Physics, pp. III.59–65.
33. K. S. Stelle, *Phys. Rev. D* **16**, 953–969 (1977).
34. V. Pravda, A. Pravdova, J. Podolsky, R. Svarc, *Phys. Rev. D* **103**, 064049 (2021).
35. C. Lanczos, *Annals of Mathematics* **39**, 842–850 (1938).

36. E. Hernández-Lorenzo, C. F. Steinwachs, *Physical Review D* **101**, 124046 (June 22, 2020).
37. A. Baruah, P. Goswami, A. Deshamukhya, *arXiv:2204.08480* (2022).
38. D. Psaltis, *Phys. Rev. D* **77**, 064006 (6 Mar. 2008).
39. D. Psaltis *et al.*, *Physical Review Letters* **125** (Oct. 2020).
40. V. Cardoso, L. C. B. Crispino, C. F. B. Macedo, H. Okawa, P. Pani, *Physical Review D* **90**, 044069 (Aug. 29, 2014).
41. J. Keir, *arXiv:1404.7036* (Sept. 7, 2016).
42. T. Bronzwaer *et al.*, *Astronomy & Astrophysics* **613**, A2 (May 2018).
43. T. Bronzwaer, Z. Younsi, J. Davelaar, H. Falcke, *Astronomy & Astrophysics* **641**, A126 (Sept. 2020).
44. E. T. Newman, A. I. Janis, *Journal of Mathematical Physics* **6**, 915–917 (June 1965).
45. S. P. Drake, R. Turolla, *Classical and Quantum Gravity* **14**, 1883–1897 (July 1997).

A. VARIATIONS OF TENSORIAL QUANTITIES

This section will provide a complete derivation of how a perturbation in the metric $g_\mu \rightarrow g_{\mu\nu} + \delta g_{\mu\nu}$ propagates to other tensorial quantities. The perturbation is to linear order, meaning that any higher order terms of $\delta g_{\mu\nu}$ will be dropped.

The inverse metric

Starting off with the inverse metric. We know it will be perturbed in a similar way as the metric,

$$g^{\mu\nu} \rightarrow g^{\mu\nu} + \delta g^{\mu\nu}, \quad (108)$$

and we can prove that the definition of the inverse metric still holds $g_{\mu\lambda}g^{\lambda\nu} = \delta_\mu^\nu$:

$$\begin{aligned} (g^{\mu\lambda} + \delta g^{\mu\lambda})(g_{\lambda\nu} + \delta g_{\lambda\nu}) &= \delta_\nu^\mu + \delta g^{\mu\lambda}g_{\lambda\nu} + g^{\mu\lambda}\delta g_{\lambda\nu} \\ &= \delta_\nu^\mu + \delta(g^{\mu\lambda}g_{\lambda\nu}) \\ &= \delta_\nu^\mu + \delta(\delta_\nu^\mu) \\ &= \delta_\nu^\mu \end{aligned} \quad (109)$$

We can use the same definition to express the perturbation of the inverse metric $\delta g^{\mu\nu}$ in terms of metric perturbation $\delta g_{\mu\nu}$ and vice versa:

$$\begin{aligned} 0 = \delta\delta_\mu^\nu &= \delta(g^{\mu\lambda}g_{\lambda\nu}) = \delta g^{\mu\lambda}g_{\lambda\nu} + g^{\mu\lambda}\delta g_{\lambda\nu} \\ &\rightarrow g^{\mu\lambda}\delta g_{\lambda\nu} = -\delta g^{\mu\lambda}g_{\lambda\nu} \quad (\times g_{\mu\kappa}) \\ &\delta g_{\kappa\nu} = -g_{\lambda\nu}g_{\mu\kappa}\delta g^{\mu\lambda} \end{aligned} \quad (110)$$

The Christoffel Symbol

With the above definitions we can now compute the variation to the Christoffel symbol

$$\begin{aligned} \Gamma_{\mu\nu}^\sigma &\rightarrow \frac{1}{2}(g^{\sigma\rho} + \delta g^{\sigma\rho})(\partial_\mu(g_{\rho\nu} + \delta g_{\rho\nu}) + \partial_\nu(g_{\mu\rho} + \delta g_{\mu\rho}) - \partial_\rho(g_{\mu\nu} + \delta g_{\mu\nu})) \\ &= \Gamma_{\mu\nu}^\sigma + \frac{1}{2}[g^{\sigma\rho}(\partial_\mu(\delta g_{\rho\nu}) + \partial_\nu(\delta g_{\mu\rho}) - \partial_\rho(\delta g_{\mu\nu})) + \delta g^{\sigma\rho}(\partial_\mu g_{\rho\nu} + \partial_\nu g_{\mu\rho} - \partial_\rho g_{\mu\nu})] \\ &= \Gamma_{\mu\nu}^\sigma + \frac{1}{2}[g^{\sigma\rho}(\partial_\mu(\delta g_{\rho\nu}) + \partial_\nu(\delta g_{\mu\rho}) - \partial_\rho(\delta g_{\mu\nu})) - g^{\sigma\lambda}g^{\epsilon\rho}(\partial_\mu g_{\rho\nu} + \partial_\nu g_{\mu\rho} - \partial_\rho g_{\mu\nu})\delta g_{\lambda\epsilon}] \\ &= \Gamma_{\mu\nu}^\sigma + \frac{1}{2}[g^{\sigma\rho}(\partial_\mu(\delta g_{\rho\nu}) + \partial_\nu(\delta g_{\mu\rho}) - \partial_\rho(\delta g_{\mu\nu})) - 2g^{\sigma\lambda}\Gamma_{\mu\nu}^\epsilon\delta g_{\lambda\epsilon}] \\ &= \Gamma_{\mu\nu}^\sigma + \frac{1}{2}[g^{\sigma\lambda}(\partial_\mu(\delta g_{\lambda\nu}) + \partial_\nu(\delta g_{\mu\lambda}) - \partial_\lambda(\delta g_{\mu\nu})) \\ &\quad - g^{\sigma\lambda}(\Gamma_{\mu\nu}^\epsilon\delta g_{\lambda\epsilon} + \Gamma_{\nu\mu}^\epsilon\delta g_{\epsilon\lambda} + \Gamma_{\nu\lambda}^\epsilon\delta g_{\mu\epsilon} - \Gamma_{\lambda\nu}^\epsilon\delta g_{\epsilon\mu} + \Gamma_{\mu\lambda}^\epsilon\delta g_{\epsilon\nu} - \Gamma_{\mu\lambda}^\epsilon\delta g_{\epsilon\nu})] \\ &= \Gamma_{\mu\nu}^\sigma + \frac{1}{2}g^{\sigma\lambda}[(\partial_\mu(\delta g_{\lambda\nu}) - \Gamma_{\mu\lambda}^\epsilon\delta g_{\epsilon\nu} - \Gamma_{\mu\nu}^\epsilon\delta g_{\lambda\epsilon}) + (\partial_\nu(\delta g_{\mu\lambda}) - \Gamma_{\nu\mu}^\epsilon\delta g_{\epsilon\lambda} - \Gamma_{\nu\lambda}^\epsilon\delta g_{\mu\epsilon}) \\ &\quad - (\partial_\lambda(\delta g_{\mu\nu}) - \Gamma_{\lambda\mu}^\epsilon\delta g_{\epsilon\nu} - \Gamma_{\lambda\nu}^\epsilon\delta g_{\mu\epsilon})] \\ &= \Gamma_{\mu\nu}^\sigma + \frac{1}{2}g^{\sigma\lambda}[\nabla_\mu\delta g_{\lambda\nu} + \nabla_\nu\delta g_{\mu\lambda} - \nabla_\lambda\delta g_{\mu\nu}] \\ &= \Gamma_{\mu\nu}^\sigma - \frac{1}{2}g^{\sigma\lambda}[g_{\lambda\alpha}g_{\nu\beta}\nabla_\mu\delta g^{\alpha\beta} + g_{\lambda\alpha}g_{\mu\beta}\nabla_\nu\delta g^{\beta\alpha} - g_{\mu\alpha}g_{\nu\beta}\nabla_\lambda\delta g^{\alpha\beta}] \\ &= \Gamma_{\mu\nu}^\sigma - \frac{1}{2}[g_{\nu\beta}\nabla_\mu\delta g^{\beta\sigma} + g_{\mu\beta}\nabla_\nu\delta g^{\beta\sigma} - g_{\mu\alpha}g_{\nu\beta}\nabla^\sigma\delta g^{\alpha\beta}] \\ &= \Gamma_{\mu\nu}^\sigma + \delta\Gamma_{\mu\nu}^\sigma \end{aligned} \quad (111)$$

After this derivation we have found that the perturbation of the Christoffel symbol takes the form

$$\delta\Gamma_{\mu\nu}^\sigma = -\frac{1}{2} [g_{\nu\beta}\nabla_\mu\delta g^{\beta\sigma} + g_{\mu\beta}\nabla_\nu\delta g^{\beta\sigma} - g_{\mu\alpha}g_{\nu\beta}\nabla^\sigma\delta g^{\alpha\beta}] . \quad (112)$$

Riemann Tensor

Next up, we can use the perturbation of the Christoffel symbol above into the definition of the Riemann tensor to compute its perturbation:

$$\begin{aligned} R_{\mu\sigma\nu}^\rho &\rightarrow \partial_\sigma(\Gamma_{\mu\nu}^\rho + \delta\Gamma_{\mu\nu}^\rho) - \partial_\nu(\Gamma_{\mu\sigma}^\rho + \delta\Gamma_{\mu\sigma}^\rho) + (\Gamma_{\mu\nu}^\epsilon + \delta\Gamma_{\mu\nu}^\epsilon)(\Gamma_{\sigma\epsilon}^\rho + \delta\Gamma_{\sigma\epsilon}^\rho) - (\Gamma_{\mu\sigma}^\epsilon + \delta\Gamma_{\mu\sigma}^\epsilon)(\Gamma_{\nu\epsilon}^\rho + \delta\Gamma_{\nu\epsilon}^\rho) \\ &= R_{\mu\sigma\nu}^\rho + \partial_\sigma(\delta\Gamma_{\mu\nu}^\rho) - \partial_\nu(\delta\Gamma_{\mu\sigma}^\rho) + \Gamma_{\mu\nu}^\epsilon\delta\Gamma_{\sigma\epsilon}^\rho + \Gamma_{\sigma\epsilon}^\rho\delta\Gamma_{\mu\nu}^\epsilon - \Gamma_{\mu\sigma}^\epsilon\delta\Gamma_{\nu\epsilon}^\rho - \Gamma_{\nu\epsilon}^\rho\delta\Gamma_{\mu\sigma}^\epsilon + (\Gamma_{\nu\sigma}^\epsilon\delta\Gamma_{\epsilon\mu}^\rho - \Gamma_{\sigma\nu}^\epsilon\delta\Gamma_{\epsilon\mu}^\rho) \\ &= R_{\mu\sigma\nu}^\rho + \partial_\sigma(\delta\Gamma_{\mu\nu}^\rho) + \Gamma_{\sigma\epsilon}^\rho\delta\Gamma_{\mu\nu}^\epsilon - \Gamma_{\mu\sigma}^\epsilon\delta\Gamma_{\nu\epsilon}^\rho - \Gamma_{\sigma\nu}^\epsilon\delta\Gamma_{\epsilon\mu}^\rho - \partial_\nu(\delta\Gamma_{\mu\sigma}^\rho) - \Gamma_{\nu\epsilon}^\rho\delta\Gamma_{\mu\sigma}^\epsilon + \Gamma_{\mu\nu}^\epsilon\delta\Gamma_{\sigma\epsilon}^\rho + \Gamma_{\nu\sigma}^\epsilon\delta\Gamma_{\epsilon\mu}^\rho \\ &= R_{\mu\sigma\nu}^\rho + \nabla_\sigma(\delta\Gamma_{\mu\nu}^\rho) - \nabla_\nu(\delta\Gamma_{\mu\sigma}^\rho) \\ &= R_{\mu\sigma\nu}^\rho + \delta R_{\mu\sigma\nu}^\rho \end{aligned} \quad (113)$$

The perturbation in the Riemann tensor due to a perturbation in the metric is thus

$$\delta R_{\mu\sigma\nu}^\rho = \nabla_\sigma(\delta\Gamma_{\mu\nu}^\rho) - \nabla_\nu(\delta\Gamma_{\mu\sigma}^\rho) . \quad (114)$$

Ricci Tensor

The perturbation in the Ricci tensor trivially follows from the result of the Riemann tensor, setting $\rho \rightarrow \sigma$,

$$\delta R_{\mu\nu} = \delta R_{\mu\sigma\nu}^\sigma = \nabla_\sigma(\delta\Gamma_{\mu\nu}^\sigma) - \nabla_\nu(\delta\Gamma_{\mu\sigma}^\sigma) . \quad (115)$$

Determinant of the metric

The last part we need in order to apply the variational principle to the Einstein Hilbert action is to express the perturbation of the determinant of the metric. For this we need to use an identity that holds for any square matrix M ,

$$\ln \det M = \text{Tr} \ln M . \quad (116)$$

Applied to our metric, $M \rightarrow g_{\mu\nu}$ and $\det M \rightarrow g$, we can vary both sides:

$$\begin{aligned} \delta(\ln g) &= \delta(\text{Tr} \ln g_{\mu\nu}) \\ \frac{1}{g}\delta g &= \text{Tr}((g_{\mu\nu})^{-1}\delta g_{\mu\nu}) \\ \delta g &= g(g^{\mu\nu}\delta g_{\mu\nu}) \\ &= -g(g^{\mu\nu}g_{\mu\alpha}g_{\nu\beta}\delta g^{\alpha\beta}) \\ &= -g(g_{\nu\beta}\delta g^{\nu\beta}) \end{aligned} \quad (117)$$

In the action, however, we have $\delta(\sqrt{-g})$. Which will follow from the chain rule:

$$\begin{aligned} \delta(\sqrt{-g}) &= \frac{1}{2\sqrt{-g}}\delta(-g) \\ &= -\frac{1}{2\sqrt{-g}}\delta(g) \\ &= -\frac{1}{2\sqrt{-g}}(-g)(g_{\mu\nu}\delta g^{\mu\nu}) \\ &= -\frac{1}{2}\sqrt{-g}g_{\mu\nu}\delta g^{\mu\nu} \end{aligned} \quad (118)$$

B. MATHEMATICA

All computations in this research were done using the proprietary software Wolfram Mathematica (version 12.3). Additional to the functions provided by the program, the package suit xAct was also used for its added support for tensor computations. In the formatting of the figures, the package SciDraw provided an extensive set of tools to achieve the desired style. The figures also called for the package MaTeX to interpret TeX code to be used within the figures.

The complete source code used in all calculations will be freely available on Github for as long as possible⁷. All generated data files as well as the full equation of motion for a axially symmetric metric will be available as well.

B.1 ”Delta Fix” for explicitly defined indices in xCoba

In the first stages of this research, a certain issue with the use of xCoba arose which halted progress for the better part of two weeks. xCoba is the part of xAct that allows for explicit definitions of the chart and metric. Subsequently, xCoba can compute all desired tensorial quantities, making it a great help in the computations. An example computation in xCoba is

```
In[1]:=Metricg[0, -sph, 0, -sph]
```

which will return the entry at g_{00} , using the chart `sph`, which has been defined as the spherical coordinates. In computing the terms of the equations of motion for Quadratic Gravity (32), we used xCoba term by term. The fourth term would for example be translated into Mathematica like

```
In[2]:=TPFev4[a_, b_] := (1/2) Simplify[Ricci[CD][c, d] Weyl[CD][a, -c, b, -d]];
```

By calling the function TPFev4 with the desired lower indexed we get the resulting equation from this tensor. The obstacle we faced was in defining the terms with a covariant derivative. Simply defining

```
In[3]:=TPFev3[a_, b_] := Simplify[CD[c][ CD[d][Weyl[CD][a, -c, b, -d]]]];
```

did not yield the correct results. The problem is that in making indices `a` and `b` explicitly defined, the covariant derivatives would no longer recognize these indices. Thus two connection terms will not be evaluated, resulting in a wrong answer. We can solve this wrong behavior by adding delta functions to delay making the indices explicit until after the covariant derivatives have been taken:

```
In[4]:=TPFev3[a_, b_] := Simplify[(delta[a, e] delta[b, f] CD[c][ CD[d][Weyl[CD][-e, -c, -f, -d]]]) // ContractBasis];
```

This fixes the unwanted behavior in most cases. For the seventh term in the equations of motion, consisting of a double covariant derivative of the Ricci scalar, this fix unfortunately did not work.

```
In[5]:=TPFev7[a_, b_]:=delta[a,c]delta[b,d]Simplify[CD[-c][CD[-d][RicciScalar[CD][]]]]//ContractBasis//Simplify;
```

takes forever to run, which it clearly should not. We can speculate that this is due to the explicit indices now being the covariant derivatives themselves. Fortunately, this term can easily be computed by hand. It might also be the case that the way xCoba is used here is not the intended way, or xCoba might not be optimized for the calculations being done. Nonetheless, xCoba has been invaluable to the computations and consequently in the making of this thesis.

⁷https://github.com/IKKUHUKKI/Thesis_QG_Kolja_Kuijpers

C. COMPLETE EXPRESSIONS

The Complete Equations of Motion

$$\begin{aligned}
H_{tt} = & (-2r^3 f(r) h(r) h'(r)^2 (29r(\alpha - 3\beta) f'(r) h'(r) + 2f(r) (29r(\alpha - 3\beta) h''(r) + (11\alpha - 78\beta) h'(r))) \\
& + r^2 h(r)^2 (9r^2(\alpha - 3\beta) f'(r)^2 h'(r)^2 + 12rf(r) h'(r) (2r(\alpha - 3\beta) f''(r) h'(r) + f'(r) (9r(\alpha - 3\beta) h''(r) \\
& + (4\alpha - 30\beta) h'(r))) - 4f(r)^2 (-9r^2(\alpha - 3\beta) h''(r)^2 + (5\alpha + 12\beta) h'(r)^2 - 2rh'(r) (6r(\alpha - 3\beta) h^{(3)}(r) \\
& + (13\alpha - 66\beta) h''(r))) - 4r^2 h(r)^3 (rf'(r) (r(\alpha - 3\beta) f''(r) h'(r) + f'(r) (3r(\alpha - 3\beta) h''(r) \\
& + (\alpha - 12\beta) h'(r))) - 2f(r) (f'(r) ((5\alpha - 6\beta) h'(r) + r ((48\beta - 13\alpha) h''(r) - 6r(\alpha - 3\beta) h^{(3)}(r))) \\
& + r (h'(r) (-r(\alpha - 3\beta) f^{(3)}(r) - 3(\alpha - 6\beta) f''(r)) - 4r(\alpha - 3\beta) f''(r) h''(r))) \\
& + 4r(\alpha - 3\beta) f(r)^2 (rh^{(4)}(r) + 4h^{(3)}(r))) + 4h(r)^4 (-4\alpha + 12\beta - r^2(\alpha - 12\beta) f'(r)^2 \\
& + 2r^3 f'(r) ((\alpha + 6\beta) f''(r) - 3\gamma) + f(r) (-72\beta + 4\alpha r^3 f^{(3)}(r) + 24\beta r^3 f^{(3)}(r) + 4r^2(\alpha + 6\beta) f''(r) \\
& - 8r(\alpha + 6\beta) f'(r) - 6\gamma r^2) + 4(\alpha + 15\beta) f(r)^2 + 6\gamma r^2) + 49r^4(\alpha - 3\beta) f(r)^2 h'(r)^4) / (24r^4 h(r)^3)
\end{aligned} \tag{119}$$

$$\begin{aligned}
H_{rr} = & (-2r^3 f(r) h(r) h'(r)^2 (3r(\alpha - 3\beta) f'(r) h'(r) + 2f(r) (3r(\alpha - 3\beta) h''(r) + (5\alpha + 12\beta) h'(r))) \\
& + 4rh(r)^3 (r^2(\alpha + 6\beta) f'(r)^2 h'(r) + 2rf(r) (h'(r) (-2r(\alpha + 6\beta) f''(r) - (\alpha + 24\beta) f'(r) + 3\gamma r) \\
& - 2r(\alpha + 6\beta) f'(r) h''(r)) + 4(\alpha + 6\beta) f(r)^2 (2h'(r) - r (rh^{(3)}(r) + 2h''(r)))) \\
& + r^2 h(r)^2 (-r^2(\alpha - 3\beta) f'(r)^2 h'(r)^2 + 4rf(r) h'(r) (r(\alpha - 3\beta) f''(r) h'(r) + 2f'(r) (r(\alpha - 3\beta) h''(r) \\
& + (2\alpha + 3\beta) h'(r))) - 4f(r)^2 (r^2(\alpha - 3\beta) h''(r)^2 + (\alpha - 48\beta) h'(r)^2 - 2rh'(r) (r(\alpha - 3\beta) h^{(3)}(r) \\
& + 6(\alpha + 3\beta) h''(r))) + 4h(r)^4 (4\alpha - 12\beta + f(r) (-72\beta + 4r^2(\alpha - 12\beta) f''(r) + 6\gamma r^2) \\
& - (r^2(\alpha - 12\beta) f'(r)^2) - 4(\alpha - 21\beta) f(r)^2 - 6\gamma r^2) + 7r^4(\alpha - 3\beta) f(r)^2 h'(r)^4) (24r^4 f(r) h(r)^4)
\end{aligned} \tag{120}$$

The equations for $X(r)$ and $Y(r)$

$$X(r) = \frac{h(\alpha - 3\beta) \left(2hrf' (2h(\alpha + 6\beta) - r(\alpha - 3\beta) h') + f \left(12h^2(\alpha + 6\beta) - r^2(\alpha - 3\beta) (h')^2 - 4hh'r(\alpha - 3\beta) \right) \right)}{(r(\alpha - 3\beta) h' - 2h(\alpha + 6\beta))^2} \tag{121}$$

$$Y(r) = \frac{2r(\alpha - 3\beta) f h^2}{2(\alpha + 6\beta) h - (\alpha - 3\beta) r h'} \tag{122}$$